

Nucleosome patterns in circulating tumor DNA reveal transcriptional regulation of advanced prostate cancer phenotypes

Navonil De Sarkar^{1,2,3,4*}, Robert D. Patton^{1,2,*}, Anna-Lisa Doebley^{1,2,5,6}, Brian Hanratty², Mohamed Adil¹, Adam J. Kreitzman^{1,2}, Jay F. Sarthy⁷, Minjeong Ko^{1,2}, Sandipan Brahma⁷, Michael P. Meers⁷, Derek H. Janssens⁷, Lisa S. Ang², Ilsa M. Coleman², Arnab Bose², Ruth F. Dumpit², Jared M. Lucas², Talina A. Nunez², Holly M. Nguyen⁸, Heather M. McClure⁹, Colin C. Pritchard^{10,11}, Michael T. Schweizer^{3,12}, Colm Morrissey⁸, Atish D. Choudhury^{9,13}, Sylvan C. Baca^{9,13}, Jacob E. Berchuck⁹, Matthew L. Freedman^{9,13}, Kami Ahmad⁶, Michael C. Haffner^{2,3,10}, R. Bruce Montgomery¹², Eva Corey⁸, Steven Henikoff^{7,14}, Peter S. Nelson^{2,3,8,11,12,†}, Gavin Ha^{1,2,11,15,†}

¹ Division of Public Health Sciences, Fred Hutchinson Cancer Center, 1100 Fairview Ave. N, Seattle, WA 98109

² Division of Human Biology, Fred Hutchinson Cancer Center, 1100 Fairview Ave. N, Seattle, WA 98109

³ Division of Clinical Research, Fred Hutchinson Cancer Center, 1100 Fairview Ave. N, Seattle, WA 98109

⁴ Department of Pathology and Prostate Cancer Center of Excellence, Medical College of Wisconsin, 8701 W Watertown Plank Road, Milwaukee, WI 53226

⁵ Molecular and Cellular Biology Graduate Program, University of Washington, 1959 NE Pacific St, Seattle WA 98195

⁶ Medical Scientist Training Program, University of Washington, 1959 NE Pacific St, Seattle WA 98195

⁷ Division of Basic Sciences, Fred Hutchinson Cancer Center, 1100 Fairview Ave. N, Seattle, WA 98109

⁸ Department of Urology, University of Washington, 1959 NE Pacific St, Seattle, WA, 98195

⁹ Dana-Farber Cancer Institute, 450 Brookline Ave, Boston, MA 02215

¹⁰ Department of Laboratory Medicine and Pathology, University of Washington, 1959 NE Pacific St, Seattle, WA 98195

¹¹ Brotman Baty Institute for Precision Medicine, 1959 NE Pacific St, Seattle, WA, 98195

¹² Division of Oncology, Department of Medicine, University of Washington

¹³ Broad Institute of MIT and Harvard, 415 Main Street, Cambridge, MA 02142

¹⁴ Howard Hughes Medical Institute, USA

¹⁵ Department of Genome Sciences, University of Washington, 1959 Pacific St, Seattle, WA, 98195

* These authors contributed equally.

† Co-senior authors.

RUNNING TITLE: Cancer phenotype classification using ctDNA

KEYWORDS: Circulating tumor DNA, liquid biopsies, castration-resistant prostate cancer, patient-derived xenografts, fragmentomics

ADDITIONAL INFORMATION

Financial support:

This research was supported by the Pacific Northwest Prostate Cancer SPORE grant (P50 CA097186) and Department of Defense Idea Development Award (W81XWH-21-1-0513). This work was also supported by the Brotman Baty Institute for Precision Medicine grants (to G.H., R.D.P., and N.D.S.), Prostate Cancer Foundation Young Investigator Awards (G.H. and N.D.S.), National Institutes of Health (K22 CA237746, R21 CA264383, and DP2 CA280624 to G.H.; R01 CA234715 and R01 CA266452 to P.S.N.; P01 CA163227 to P.S.N., E.C., and C.M.; R01 CA251555 to M.L.F.; K99 GM138920 to S.B.; K99 GM140251 to M.P.M.), Department of Defense (W81XWH-18-1-0406 to P.S.N.; W81XWH-17-1-0380 to N.D.S.; W81XWH-18-0756, W81XWH-18-1-0356, PC170510, PC170503P2, PC200262P to C.C.P.;

W81XWH-20-1-0118 to J.E.B.; W81XWH-20-1-0084 to A.B.). Support was also provided by the Prostate Cancer Foundation, the Institute for Prostate Cancer Research, V Foundation Scholar Grants (to G.H. and M.C.H.), Fund for Innovation in Cancer Informatics Major Grant (to G.H.); Doris Duke Charitable Foundation and Safeway Foundation (to M.C.H.); Wong Family Award in Translational Oncology and Dana-Farber Cancer Institute Medical Oncology grant (to A.D.C.); H.L. Snyder Medical Research Foundation, the Cutler Family Fund for Prevention and Early Detection, and Claudia Adams Barr Program for Innovative Cancer Research (to M.L.F.); ASCO Young Investigator Award, Kure It Cancer Research Foundation, and PhRMA Foundation (to S.C.B.). This research was also supported in part by the NIH/NCI Cancer Center Support Grant (P30 CA015704) and Scientific Computing Infrastructure (ORIP Grant S10OD028685).

Correspondence:

Gavin Ha, Ph.D.
Fred Hutchinson Cancer Center
1100 Fairview Ave. N,
Seattle, WA 98109
206-667-2802
gha@fredhutch.org

Peter S. Nelson, M.D.
Fred Hutchinson Cancer Center
1100 Fairview Ave. N,
Seattle, WA 98109
206-667-3377
pnelson@fredhutch.org

Conflict of interest disclosure:

G.H., A-L.D., N.D.S., R.D.P., P.S.N.: These authors have filed pending patent applications on methodologies developed in this manuscript (PCT/US2002/024082 and provisional patent USSN: 63/353,331).

P.S.N.: Served as a paid consultant to Janssen, Astellas, Pfizer, and Bristol Myers Squibb in work unrelated to the present study.

B.M.: Has institutional funding from Clovis, Janssen, Astellas, BeiGene, and AstraZeneca.

E.C.: Received research funding under institutional SRA from Janssen Research and Development, Bayer Pharmaceuticals, KronosBio, Forma Pharmaceuticals Foghorn, Gilead, Sanofi, AbbVie, and GSK for work unrelated to the present study.

M.L.F.: Serves as a consultant to and has equity in Nuscan Diagnostics. This activity is outside of the scope of this manuscript. M.L.F. has a pending patent for detecting NEPC using DNA methylation.

M.T.S.: Paid consultant and/or received Honoraria from Sanofi, AstraZeneca, PharmaIn and Resverlogix. He has received research funding to his institution from Zenith Epigenetics, Bristol Myers Squibb, Merck,

Immunomedics, Janssen, AstraZeneca, Pfizer, Madison Vaccines, Hoffman-La Roche, Tmunity, SignalOne Bio and Ambrx, Inc.

All other authors declare no competing interests.

1 **ABSTRACT**

2 Advanced prostate cancers comprise distinct phenotypes, but tumor classification remains
3 clinically challenging. Here, we harnessed circulating tumor DNA (ctDNA) to study tumor
4 phenotypes by ascertaining nucleosome positioning patterns associated with transcription
5 regulation. We sequenced plasma ctDNA whole genomes from patient-derived xenografts
6 representing a spectrum of androgen receptor active (ARPC) and neuroendocrine (NEPC)
7 prostate cancers. Nucleosome patterns associated with transcriptional activity were reflected in
8 ctDNA at regions of genes, promoters, histone modifications, transcription factor binding, and
9 accessible chromatin. We identified the activity of key phenotype-defining transcriptional
10 regulators from ctDNA, including AR, ASCL1, HOXB13, HNF4G, and GATA2. To distinguish
11 NEPC and ARPC in patient plasma samples, we developed prediction models that achieved
12 accuracies of 97% for dominant phenotypes and 87% for mixed clinical phenotypes. While
13 phenotype classification is typically assessed by immunohistochemistry or transcriptome
14 profiling from tumor biopsies, we demonstrate that ctDNA provides comparable results with
15 diagnostic advantages for precision oncology.

16

17 **STATEMENT OF SIGNIFICANCE**

18 This study provides insights into the dynamics of nucleosome positioning and gene regulation
19 associated with cancer phenotypes that can be ascertained from ctDNA. New methods for
20 classification in phenotype mixtures extend the utility of ctDNA beyond assessments of somatic
21 DNA alterations with important implications for molecular classification and precision oncology.

22 INTRODUCTION

23 Metastatic castration-resistant prostate cancer (mCRPC) describes the stage in which the
24 disease has developed resistance to androgen ablation therapies and is lethal (1). Androgen
25 receptor signaling inhibitors (ARSI), designed for the treatment of CRPC, repress androgen
26 receptor (AR) activity and improve survival, but these therapies eventually fail (2,3). Since the
27 adoption of ARSI as standard-of-care for mCRPC, there has been a prominent increase in the
28 frequency of treatment-resistant tumors with neuroendocrine (NE) differentiation and features of
29 small-cell carcinomas (4–7). These aggressive tumors may develop through a resistance
30 mechanism of trans-differentiation from AR-positive adenocarcinoma (ARPC) to NE prostate
31 cancer (NEPC) that lack AR activity (4,7–10). Additional phenotypes can also arise based on
32 expression of AR activity and NE genes, including AR-low prostate cancer (ARLPC) and
33 double-negative prostate cancer (DNPC; AR-null/NE-null) (5,11–13). Distinguishing prostate
34 cancer subtypes has clinical relevance in view of differential responses to therapeutics, but the
35 need for a biopsy to diagnose tumor histology can be challenging: invasive procedures are
36 expensive and accompanied by morbidity, a subset of tumors are not accessible to biopsy, and
37 bone sites pose particular challenges with respect to sample quality (7,14).

38 Circulating tumor DNA (ctDNA) released from tumor cells into the blood as cell-free DNA
39 (cfDNA) is a non-invasive “liquid biopsy” solution for accessing tumor molecular information.
40 The analysis of ctDNA to detect mutation and copy-number alterations has served to classify
41 genomic subtypes of CRPC tumors (4,15–21). However, the defining losses of *TP53* and *RB1* in
42 NEPC do not always lead to NE trans-differentiation (7,22). Rather, ARPC and NEPC tumors
43 are associated with distinct reprogramming of transcriptional regulation (8,9,23). Methylation
44 analysis of cfDNA in mCRPC to profile the epigenome shows promise for distinguishing
45 phenotypes, but requires specialized assays such as bisulfite conversion, enzymatic treatment,
46 or immunoprecipitation (24–27).

47 The majority of cfDNA represents DNA protected by nucleosomes when released from dying
48 cells into circulation, leading to DNA fragmentation that is reflective of the non-random
49 enzymatic cleavage by nucleases (28,29). Emerging approaches to analyze cfDNA
50 fragmentation patterns from plasma for studying cancer can be performed directly from standard
51 whole genome sequencing (WGS) (30–35). cfDNA fragments primarily have a characteristic
52 size of ~167 bp, consistent with protection by a single core nucleosome octamer and histone
53 linkers, but the size distribution may vary between healthy individuals and cancer patients (36–

54 39). Recent studies have demonstrated that the nucleosome occupancy in cfDNA at the
55 transcription start site (TSS) and transcription factor binding site (TFBS) can be used to infer
56 gene expression and transcription factor (TF) activity from cfDNA (40–42). However,
57 nucleosome positioning and spacing are dynamic in active and repressed gene regulation (43–
58 45). A detailed understanding of the nucleosome patterns and accessible chromatin associated
59 with transcriptional regulation in tumor phenotypes has not been fully explored in cfDNA.

60 The objective of this study is to determine if ctDNA could be used to accurately classify tumor
61 phenotypes in men with mCRPC. A major challenge for ctDNA analysis is the low tumor content
62 (tumor fraction) in patient plasma samples. By contrast, plasma from patient-derived xenograft
63 (PDX) models may contain nearly pure human ctDNA after bioinformatic exclusion of mouse
64 DNA reads (37,39,46). This provides a resource that is ideal for studying the properties of
65 ctDNA, developing new analytical tools, and validating both genetic and phenotypic features by
66 comparison to matching tumors. In this study, we performed WGS of ctDNA from mouse plasma
67 across 24 CRPC PDX lines with diverse phenotypes. Applying newly developed computational
68 methods, we comprehensively interrogated the nucleosome patterns in ctDNA across genes,
69 regulatory loci, TFBSs, TSSs, and open chromatin sites to reveal transcriptional regulation
70 associated with mCRPC phenotypes. Finally, we designed two probabilistic models to
71 accurately classify treatment-resistant tumors into divergent phenotypes and to estimate the
72 phenotype heterogeneity within a ctDNA sample. We then validated the performance of these
73 models in 159 plasma samples from three mCRPC patient cohorts. Overall, these results
74 highlight that transcriptional regulation of tumor phenotypes can be ascertained from ctDNA and
75 has potential utility for diagnostic applications in cancer precision medicine.

76 **RESULTS**

77 **Comprehensive resource of matched tumor and liquid biopsies from patient derived** 78 **xenograft (PDX) models of advanced prostate cancer**

79 To develop approaches for the accurate classification of mCRPC using ctDNA, we evaluated 26
80 models from the LuCaP PDX series of advanced prostate cancer with well-defined phenotypes
81 determined by whole transcriptome RNAseq and immunohistochemical assays for protein
82 expression (47). The models consisted of 18 classified as ARPC, two classified as AR-low and
83 NE-negative prostate cancer (ARLPC), and six classified as NEPC (**Figure 1A**). For each PDX
84 line, we pooled mouse plasma (1.9 – 3.0 mL) from four to eight mice (mean tumor volume range
85 393-1239 mm³), extracted cfDNA, and performed deep whole genome sequencing (WGS; mean

86 38.4x coverage, range 21 – 85x) (**Methods, Supplementary Table S1**). We used bioinformatic
87 subtraction of mouse sequenced reads to obtain nearly pure human ctDNA data (**Methods**). We
88 observed that 25 lines had human ctDNA comprising more than 10% of the sample (mean
89 52.9%, range 10.6 – 96%) with NEPC samples having significantly higher human fractions
90 (mean 85.1%, range 77.1 – 96%, two-tailed Mann-Whitney U test $p = 9.6 \times 10^{-4}$) (**Figure 1B,**
91 **Supplementary Table S1**). After subsequent filtering by human ctDNA sequencing coverage,
92 24 PDX lines remained for further analysis (16 ARPC, 6 NEPC, 2 ARLPC; mean 20.5x, range
93 3.8 – 50.6x, **Supplementary Table S1**). In the matching tumors, we performed Cleavage Under
94 Targets and Release using Nuclease (CUT&RUN) to profile H3K27ac, H3K4me1, and
95 H3K27me3 histone post-translational modifications (PTMs) (48,49) (**Supplementary Fig. S1**).
96 We hypothesized that nucleosome organization inferred from ctDNA reflects the transcriptional
97 activity state regulated by histone PTMs (50).

98 To study transcriptional regulation in mCRPC phenotypes from ctDNA, we interrogated four
99 different features: (i) local promoter coverage, (ii) nucleosome positioning, (iii) fragment size
100 analysis, and (iv) composite TFBSs plus open chromatin sites analysis using the Griffin
101 framework (51) (**Figure 1A, Methods**). First, we analyzed three different local regions within
102 ctDNA: all gene promoters and gene bodies and sites of histone PTMs guided by CUT&RUN
103 analysis. For each of the three local regions, we extracted features of nucleosome periodicity
104 using a nucleosome phasing approach and computed the fragment size variability. For promoter
105 regions, we also computed the coverage at the transcription start site (TSS). Next, we analyzed
106 ctDNA at transcription factor binding sites (TFBSs) and open chromatin regions. For each
107 transcription factor (TF), ctDNA coverage at TFBSs were aggregated into composite profiles
108 representing the inferred activity (42,51). Similarly, features in the composite profiles of
109 phenotype-specific open chromatin regions were extracted for analyzing the signatures of
110 chromatin accessibility in ctDNA. Altogether, we assembled a multi-omic sequencing dataset
111 from matching tumor and plasma for a total of 24 PDX lines, making this a unique molecular
112 resource and platform for developing transcriptional regulation signatures of tumor phenotype
113 prediction from ctDNA.

114 **Characterizing transcriptional activity of AR and ASCL1 in PDX phenotypes through** 115 **analysis of tumor histone modifications and ctDNA**

116 We sought to further characterize the transcriptional activity in different tumor phenotypes by
117 studying epigenetic regulation via histone PTMs. We identified broad peak regions for H3K4me1

118 (median of 17,643 regions, range 1,894 – 64,934), H3K27ac (median 7,093, range 1610 -
119 34,047), and H3K27me3 (median 8,737, range 2,024 - 42,495) in the tumors of the 24 PDX
120 lines and an additional nine LuCaP PDX lines where only tumors were available (total of 25
121 ARPC, 2 ARLPC, and 6 NEPC) (**Methods, Supplementary Fig. S1, Supplementary Table S2**).
122 Using unsupervised clustering and principal components analysis (PCA), we identified putative
123 active regulatory regions of enhancers and promoters (H3K27ac, H3K4me1) and gene
124 repressive heterochromatic marks (H3K27me3) that were specific to ARPC, ARLPC, and NEPC
125 phenotypes (52) (**Supplementary Fig. S2A**).

126 AR and ASCL1 are two key differentially expressed TFs with known regulatory roles in ARPC
127 and NEPC phenotypes, respectively (9,53–55). When inspecting AR binding sites in ARPC
128 tumors, we observed increased signals from flanking nucleosomes with H3K27ac PTMs
129 compared to the other phenotypes (area under mean peak profile of 18.46 vs. 15.08 in ARLPC
130 and 10.63 in NEPC, **Figure 2A, Supplementary Fig. S2B, Methods**). We also observed the
131 strongest signals at the nucleosome depleted region (NDR) in ARPC for H3K27ac (1.54
132 coverage decrease vs. 0.78 for ARLPC and 0.41 for NEPC). Conversely, in NEPC tumors, we
133 observed stronger signals at nucleosomes with H3K27ac PTMs flanking ASCL1 binding sites
134 (area under mean peak profile 62.65 vs. 29.18 for ARLPC and 10.83 for ARPC), and stronger
135 NDR signals (2.26 coverage decrease vs. 0.19 for ARPC and 0.37 for ARLPC). We observed
136 similar trends for H3K4me1 PTMs in the LuCaP PDX lines (**Supplementary Fig. S2C**).

137 We analyzed the ctDNA composite coverage profiles at 1,000 consensus TFBSs to evaluate
138 nucleosome accessibility, where lower normalized central (± 30 bp window) mean coverage
139 across these sites suggests more nucleosome depletion (**Methods**). For AR TFBSs, we
140 observed the strongest signal for nucleosome depletion in ARPC, as indicated by the lowest
141 mean central coverage (average 0.64, n=16), compared to moderate signals for ARLPC
142 (average 0.88, n=2), and weakest signals for NEPC (average 0.95, n=6) (**Figure 2B**).
143 Conversely, the composite coverage profile at ASCL1 TFBSs showed the strongest nucleosome
144 depletion for NEPC samples (mean central coverage 0.69) compared to ARLPC (0.86) and
145 ARPC (0.88) (**Figure 2C**). These observations were consistent with the differential binding
146 activity by AR and ASCL1 in their respective phenotypes from tumor tissue (**Figure 2A**). We
147 confirmed the same differential binding activity trends when analyzing TFBSs identified from
148 other primary tissue sources (9,56,57) (**Supplementary Fig. S3A-B**). We also noted that the
149 composite TFBS coverage patterns in ctDNA resembled the NDR flanked by nucleosomes with
150 H3K27ac and H3K4me1 modifications inferred by CUT&RUN (**Figure 2A, Supplementary Fig.**

151 **S2B-C**). Together, these results suggest that the nucleosome depletion in ctDNA at AR and
152 ASCL1 binding sites represents active TF binding and regulatory activity in specific prostate
153 PDX tumor phenotypes.

154 **Nucleosome patterns at gene promoters inferred from ctDNA are consistent with** 155 **transcriptional activity for phenotype-specific genes**

156 We selected 47 genes comprising 12 ARPC and 35 NEPC lineage markers established
157 previously (4,5,58,59) and confirmed their phenotype associations by RNA-Seq from the PDX
158 tumors (**Figure 2D, Supplementary Table S3, Methods**). To assess the activity of these genes
159 from ctDNA, we analyzed the ctDNA fragment size in TSSs (± 1 kb window) and gene bodies
160 and found that the differential size variability between phenotypes was positively correlated with
161 relative expression (Spearman's $r = 0.844$, $p = 9.4 \times 10^{-14}$, **Figure 2E, Supplementary Fig. S4,**
162 **Supplementary Table S2, Methods**). However, closer inspection of ctDNA coverage patterns
163 at promoters revealed consistent nucleosome organization for transcription activity and
164 repression (40,60–62) (**Figure 2D**). Therefore, we grouped the genes based on differential
165 signals in H3K27me3 histone PTMs, which are linked with polycomb repressive complex
166 mediated regulation and chromatin compaction (63).

167 For 25 genes without differential H3K27me3 peaks (Group 1), including AR, KLK3 and ASCL1,
168 we observed nucleosome depletion at the TSS consistent with presence of active PTMs, such
169 as for AR (mean coverage 0.47, $n=16$) in ARPC and ASCL1 (0.30, $n=6$) in NEPC samples
170 (**Figure 2F, Supplementary Fig. S5**). By contrast, we observed increased coverage at the TSS
171 of AR (1.08) in NEPC and ASCL1 (0.42) in ARPC, which supports nucleosome depletion in the
172 absence of PTMs and inactive transcription. For 22 genes with differential H3K27me3 peaks
173 (Group 2), including INSM1, CHGB and SRRM4, we observed relatively consistent increase in
174 nucleosome occupancy and phasing in the TSS as well as in the gene body for ~50% of the
175 genes (**Figure 2G, Supplementary Fig. S6**). The neuronal signaling genes in this group, such
176 as UNC13A and INSM1, had reduced signals for the stable nucleosome dyad position,
177 consistent with the heterogeneous ('fuzzy') nucleosome patterns described for actively
178 transcribed genes (44,64). Interestingly, while UNC13A was active in NEPC tumors, we did not
179 detect H3K27ac nor H3K4me1 PTM marks in the regulatory loci of this gene (**Supplementary**
180 **Fig. S7A-B**). These results illustrate that ctDNA analysis can reveal patterns that are consistent
181 with different modalities of transcriptional regulation by histone modifications for key genes that
182 define prostate cancer phenotypes.

183 **Phasing analysis in ctDNA reveals nucleosome periodicity associated with**
184 **transcriptional activity between CRPC phenotypes**

185 Regions of inactive or repressed transcription are expected to have stably bound nucleosomes,
186 resulting in more periodic phasing in the gene body (61,65,66). Conversely, actively transcribed
187 regions may exhibit overall disordered phasing in the gene body due to fast nucleosome
188 turnover, resulting in relatively aperiodic patterns with highly varied protection from nucleases
189 along the gene (67). To systematically quantify inter-nucleosomal spacing and predict
190 nucleosome phasing, we developed TritonNP, a tool utilizing Fourier transforms and band-pass
191 filters on GC-corrected ctDNA coverage to isolate frequency components corresponding to
192 phased nucleosomes (**Figure 3A, Supplementary Fig. S8A-B, Methods**). This approach
193 allows for calling phased nucleosome dyad positions to generate an average inter-nucleosome
194 distance from the originating cells, encapsulating potential heterogeneity in nucleosome
195 occupancy and stability. In PDX ctDNA, we observed a larger mean phased-nucleosome
196 distance across 17,946 genes in the ARPC lines compared to the NEPC lines (median 291.1 bp
197 vs. 282.6 bp, $p = 0.027$; two-tailed Mann-Whitney U test, **Figure 3B**). The phased nucleosome
198 distance was also negatively correlated with the mean cell cycle progression (CCP) score
199 (Spearman's $\rho = -0.563$, $p = 0.006$, **Figure 3C, Methods**). These results suggest that
200 increased nucleosome periodicity in NEPC ctDNA may reflect the condensed chromatin in
201 hyperchromatic nuclei of NE cells (14), and the phasing analysis may have potential utility for
202 assessing tumor proliferation and aggressiveness (68).

203 To model the relationship between nucleosome phasing and transcriptional activity more directly,
204 we further extracted the frequency components corresponding to the inter-dyad distances of
205 “stable” nucleosomes (180 – 210 bp) and a “baseline” component (150 – 180 bp) for
206 normalization between samples of differing depths (69). We then computed the ratio of the
207 mean frequency amplitudes between these components, which we designated the nucleosome
208 phasing score (NPS), where a higher score corresponded to more ordered nucleosome phasing
209 and repressed transcription. As an example, HOXB13, which is transcriptionally inactive in
210 NEPC, had higher overall GC-corrected coverage (mean 56.85 depth) and a phased
211 nucleosome distance of 249 bp with a 1.93 NPS in the LuCaP 93 NEPC PDX (**Figure 3A**). By
212 contrast, HOXB13 is actively transcribed in ARPC and had lower coverage (mean 13.54 depth)
213 and a more disordered phased-nucleosome distance of 332 bp with a 1.63 NPS in the LuCaP
214 136 ARPC PDX. When assessing the 47-prostate cancer phenotype marker genes, we
215 observed that the mean NPS for the 35 NE genes was lower in NEPC lines compared to ARPC

216 (median NPS 1.95 vs. 2.21, $p = 0.134$; two-tailed Mann-Whitney U test, **Figure 3D**); although
217 this was not statistically significant, it was consistent with their active transcription. Conversely,
218 the mean NPS for the 12 AR-regulated genes was lower in ARPC lines compared to NEPC
219 (median NPS 1.82 vs 2.13, $p = 0.070$; two-tailed Mann-Whitney U test). In particular, 26 (74%)
220 of the NE genes had lower NPS in NEPC compared to ARPC (\log_2 fold-change [ARPC:NEPC] $>$
221 0), including seven genes (ASCL1, CHGB, CHRN2, GRP, MYCL, XKR7, NEUROD1) that
222 were statistically significant ($p < 0.05$); ten (83%) of the AR-regulated genes had lower NPS in
223 ARPC (\log_2 fold-change < 0), with TMPRSS2 being statistically significant (**Figure 3E**,
224 **Supplementary Table S3**). These results illustrate that the NPS captured signals distinguishing
225 key lineage-specific gene markers.

226 **Inferred TF activity from analysis of nucleosome accessibility at TFBSs in ctDNA** 227 **confirms key regulators of tumor phenotypes**

228 To characterize the regulation of prostate tumor phenotype lineages, we considered
229 nucleosome accessibility at TFBSs in PDX ctDNA for 338 TFs from the Gene Transcription
230 Regulation Database (GTRD)(70) (**Methods**). First, we identified 108 TFs out of the 338 that
231 were differentially expressed between ARPC and NEPC PDX tumors by RNAseq
232 (**Supplementary Fig. S9, Supplementary Table S3, Methods**). Through unsupervised
233 hierarchical clustering of composite TFBS central coverage values for these 108 TFs, we
234 observed distinct groups of TFs in PDX ctDNA (**Figure 3F**). Of these 108 TFs, 38 had
235 significantly different accessibility in ctDNA between ARPC and NEPC phenotypes (two tailed
236 Mann-Whitney U test, Benjamini-Hochberg adjusted $p < 0.05$, **Supplementary Table S3**). Most
237 of these TFs (27/38 [71%]) had differential inferred accessibility in ctDNA that was consistent
238 with their up-regulation in the same phenotype by tumor mRNA expression, although some TFs
239 (11/38, [29%]) did not show this trend (**Figure 3F, Supplementary Fig. S10**). A comparison of
240 TFBS between paralogous TFs revealed that the binding sites used in the analysis had limited
241 overlap (median 18.3%, range 0-81.2%), suggesting that many of the TFs may have some
242 independent inferred accessibility (**Supplementary Fig. S11, Supplementary Table S3**). For
243 paralogs with high TFBS overlap ($\geq 19\%$), such as AR, NR3C1 and PGR, we noted only a
244 subset of TFs were expressed in one phenotype.

245 REST had the largest difference in accessibility as supported by a decrease in coverage within
246 ARPC models compared to NEPC (\log_2 fold-change -0.77 , adjusted $p = 5.7 \times 10^{-4}$,
247 **Supplementary Fig. S12A, Supplementary Table S3**). FOXA1, and GRHL2 binding sites were

248 significantly more accessible in ARPC (and ARLPC) samples compared to NEPC (\log_2 fold-
249 change < -0.57 , adjusted $p < 1.3 \times 10^{-3}$). AR, HOXB13, and NKX3-1 had higher accessibility in
250 ARPC compared to NEPC (\log_2 fold-change < -0.37 , adjusted $p < 1.3 \times 10^{-3}$), but with only
251 moderate accessibility in ARLPC, as expected. We also observed a group of TFs that followed
252 a similar trend, including nuclear hormone receptors (NR2F2, RARG), pioneer factor GATA2,
253 and nuclear factors HNF4G and HNF1A (\log_2 fold-change < -0.10 , adjusted $p < 0.027$,
254 **Supplementary Fig. S12A**).

255 For factors that had higher accessibility in NEPC models compared to ARPC and ARLPC,
256 ASCL1 had the largest TFBS coverage difference (\log_2 fold-change 0.36, adjusted $p = 5.7 \times 10^{-4}$,
257 **Figure 2C, Figure 3F**). Other TFs, including RUNX1, BCL11B, POU3F2, NEUROG2, and
258 SOX2 also had sites with higher accessibility in NEPC (\log_2 fold-change > 0.06 , adjusted $p <$
259 0.048 , **Supplementary Fig. S12B**), although the difference was modest. Other notable factors
260 such as MYC and ETS transcription family genes (ETV4, ETV5, ETS1, ETV1) had high
261 accessibility across all phenotypes, while NEUROD1, RUNX3, and TP63 sites were
262 inaccessible in nearly all samples. Furthermore, we considered restricting the analysis to 20 TFs
263 with TFBSs that were observed in prostatic tissue and cell lines and were also differentially
264 expressed in the PDX tumors by RNAseq (**Methods**). However, while hierarchical clustering
265 distinguished PDX tumor phenotypes, key NEPC-defining markers, such as ASCL1, were
266 omitted from this analysis as ChIP-seq for many NEPC-defining markers had not been
267 performed on prostate lineage samples in GTRD (**Supplementary Fig. S13**). Overall, we
268 identified the accessibility of known prostate cancer regulators, including ASCL1, HNF4G,
269 HNF1A, GATA2 and SOX2 (71–73), that have not been shown before from ctDNA analysis in
270 these tumor phenotypes.

271 **Phenotype-specific open chromatin regions (ATAC-Seq) in PDX tumor tissue are** 272 **reflected in ctDNA profiles of nucleosome accessibility**

273 Nucleosome profiling from cfDNA sequencing analysis has shown agreement with overall
274 chromatin accessibility in tumor tissue (38,42,74); however, its application for distinguishing
275 tumor phenotypes has been limited. We hypothesized that due to lack of protection from
276 nucleases, regions of open chromatin would be under-represented in ctDNA assays. We
277 investigated the use of ATAC-Seq data from tumor tissue for 10 LuCaP PDX lines (5 ARPC and
278 5 NEPC) to inform phenotype-related differences in chromatin accessibility (9). We defined an
279 initial set of 28,765 ARPC and 21,963 NEPC differential consensus open chromatin regions

280 which we further restricted to those that overlapped TFBSs for 338 TFs, resulting in 15,879
281 ARPC and 11,692 NEPC sites (**Methods, Figure 4A**). For ARPC-specific open chromatin sites,
282 we observed decreased overall composite site coverage (+/- 1 kb window) and central coverage
283 (+/- 30 bp) in the ctDNA for ARPC PDX lines (mean central coverage 0.75, n=16) compared to
284 NEPC lines (mean 0.96, n=6) and cfDNA from healthy human donors (mean 0.97, n=14)
285 (**Figure 4B, Supplementary Table S3, Methods**). Conversely, for NEPC-specific open
286 chromatin sites, coverage was decreased in ctDNA for NEPC lines (mean 0.89) compared to
287 ARPC lines (mean 1.01) and healthy donors cfDNA (mean 1.00) (**Figure 4C, Supplementary**
288 **Table S3**). Coverage patterns were discernable between phenotypes for as few as 100 sites,
289 suggesting that even a smaller subset of open chromatin regions may still be informative
290 (**Supplementary Fig. S14A-B**). These results confirmed that tumor tissue chromatin
291 accessibility can be corroborated in ctDNA and that ARPC and NEPC phenotypes have distinct
292 ctDNA coverage profiles at these sites.

293 **Comprehensive evaluation of ctDNA features across genomic contexts for CRPC** 294 **phenotype classification**

295 To assess the utility of ctDNA nucleosome profiling for informing prostate cancer phenotype
296 classification, we systematically evaluated four groups of global genome-wide ctDNA features:
297 phasing, fragment sizes, local coverage profiling, and composite site coverage profiling (**Figure**
298 **1A**). From principal components analysis (PCA), we observed distinct feature signals between
299 ARPC and NEPC phenotypes for composite TFBS coverage of TFs, NPS of the 47 phenotype
300 marker genes, and fragment size variability at global sites of PTMs (**Figure 4D, Supplementary**
301 **Fig. S15A, Supplementary Table S4, Methods**). In addition to these features, we also
302 included previously reported features, including short-long fragment ratio and local coverage
303 patterns at the TSS (max wave height between -120bp to 195bp) (30,41) (**Methods**).

304 We then quantitatively evaluated all combinations of coverage, phasing, and fragment size
305 features for different genomic contexts to investigate their potential to classify ARPC and NEPC
306 phenotypes. For each feature set, we conducted 100 iterations of stratified cross-validation
307 using a supervised machine learning classifier (XGBoost) on ctDNA samples from the ARPC
308 and NEPC models and computed the area under the receiver operating characteristic curve
309 (AUC) (**Methods**). First, we evaluated an established set of 10 genes associated with AR
310 activity (5,12). We observed that the phased nucleosome distance at H3K27ac sites and the
311 central coverage at TSSs had moderate predictive performance (AUC 0.88) (**Supplementary**

312 **Fig. S15B, Supplementary Table S4).** For the set of 47 phenotype markers, the NPS of gene
313 bodies was most predictive (AUC 0.98) (**Supplementary Fig. S15C, Supplementary Table S4**).
314 When considering all PTM sites, promoters, genes, TFs, and open chromatin regions, the best
315 performing features included mean fragment size at H3K4me1 sites (n=9,750, AUC 1.0) and
316 promoter TSSs (n=17,946, AUC 1.0), and both open chromatin composite site features (AUC
317 1.0) (**Figure 4E, Supplementary Table S4**).

318 **Accurate classification of ARPC and NEPC phenotypes from patient plasma using a** 319 **probabilistic model informed by PDX ctDNA analysis**

320 An important consideration and challenge in analyzing plasma from patients is the presence of
321 cfDNA released by hematopoietic cells, which leads to a lower ctDNA fraction (i.e., tumor
322 fraction). Furthermore, the small patient cohorts with available tumor phenotype information
323 make supervised machine learning approaches suboptimal. Therefore, we developed ctdPheno,
324 a probabilistic model to classify ARPC and NEPC from an individual plasma sample, accounting
325 for the tumor fraction (**Figure 5A, Methods**). We focused on the phenotype-specific open
326 chromatin composite site features and used the PDX plasma ctDNA signals (27,571 total sites,
327 **Figure 4B-C, Supplementary Table S3**) to inform the model. The model produces a
328 normalized prediction score that represents the estimated signature of ARPC (lower values) and
329 NEPC (higher values). We applied this method to benchmarking datasets generated by
330 simulating varying tumor fractions and sequencing coverages using five ARPC and NEPC PDX
331 ctDNA samples each, and healthy donor plasma cfDNA (**Supplementary Figure 15D,**
332 **Methods**). We achieved a 1.0 AUC at 25X coverage down to 0.01 tumor fraction, 1.0 AUC at
333 1X down to 0.2 tumor fraction, and 1.0 AUC at 0.2x coverage at 0.3 tumor fraction, suggesting a
334 possible upper-bound performance for classifying samples with lower tumor fraction in plasma
335 (**Figure 5B, Supplementary Table S4**).

336 To test the performance of ctdPheno on patient samples, we analyzed a published dataset of
337 ultra-low-pass whole genome sequencing (ULP-WGS) of plasma cfDNA (mean coverage 0.52X,
338 range 0.28-0.92X) from 101 mCRPC patients comprising 80 adenocarcinoma (ARPC) and 21
339 NEPC samples (DFCI cohort I) (25). Using ctdPheno, which was unsupervised and used
340 parameters informed only by the PDX analysis, we achieved an overall AUC of 0.96 (**Figure 5C,**
341 **Supplementary Table S5**). The performance was 0.97 AUC and 0.76 AUC when considering
342 samples with high (≥ 0.1) and low (< 0.1) tumor fraction, respectively, and 0.83 AUC when using
343 only 2000 sites for analysis (**Supplementary Fig. S16A-B**). We identified an optimal overall

344 performance at 97.5% specificity (ARPC) and 90.4% sensitivity (NEPC) which corresponded to
345 the prediction score of 0.3314 (**Figure 5C**). These results were concordant (92.1%) with
346 phenotype classification by cfDNA methylation on the same plasma samples (**Supplementary**
347 **Fig. S16C, Supplementary Table S5**). In another published dataset of 11 mCRPC samples
348 from 6 patients who had high PSA, treatment with ARSI, or both (DFCI cohort II) (75,76), the
349 model correctly classified patients as ARPC in 8 (73%) ULP-WGS (~0.1x) samples when using
350 the optimal score cutoff (**Supplementary Fig. S16D, Supplementary Table S5**).

351 Next, we analyzed 61 clinical plasma samples from 31 CRPC patients with ARPC, NEPC, and
352 mixed phenotypes that are representative of typical clinical histories (UW Cohort,
353 **Supplementary Table S5**). We performed ULP-WGS of cfDNA and selected 47 samples (26
354 ARPC, 5 NEPC, and 16 mixed phenotype) from 27 patients based on having greater than 3%
355 estimated tumor fraction (**Supplementary Table S5, Methods**). For the 26 samples with ARPC
356 clinical phenotype, ctdPheno correctly classified 22 (85%) samples with ARPC-dominant clinical
357 phenotype and all five (100%) samples with NEPC-dominant clinical phenotype using the score
358 cutoff of 0.3314 (**Figure 5D**). For the remaining 16 samples with clinical histories or tumor
359 histologies that reflected mixed phenotypes such as a tumor with AR-positive adenocarcinoma
360 intermixed with NEPC, the classification results were variable (**Figure 5D, Supplementary**
361 **Table S5, Supplementary Fig. S17**). Overall, we achieved an accuracy of 87% for ULP-WGS
362 data of ctDNA samples with dominant clinical phenotypes, but the variable predictions for mixed
363 phenotype samples underscore the complexities associated with tumor heterogeneity in the
364 setting of metastatic disease.

365 **Quantifying ARPC and NEPC phenotype heterogeneity within individual patient plasma** 366 **ctDNA**

367 Phenotype heterogeneity may arise in the clinical setting, particularly when trans-differentiation
368 can lead to a mixture of ARPC and NEPC cells or lesions. To account for and predict phenotype
369 mixtures within a patient ctDNA sample, we developed Keraon, an analytical model that
370 estimates the proportions of phenotypes from WGS using the same ctDNA features as
371 ctdPheno (**Figure 5E, Methods**). First, we evaluated Keraon using a benchmark dataset
372 generated for simulating varying tumor fractions and proportions of ARPC-NEPC mixtures at
373 25x coverage using PDX ctDNA and healthy donor cfDNA data (**Figure 5F, Methods**). In 810
374 simulated phenotype mixtures, we observed the estimated total NEPC fraction was consistent
375 with expected proportions (Pearson's $r=0.884$) with a mean absolute error (MAE) of 0.028,

376 highlighting the method's potential for accurate estimation of emergent phenotypes in mixed
377 histology samples (**Figure 5G, Supplementary Table S5**). Next, we evaluated Keraon for
378 classifying NEPC in DFCI Cohort I and observed the highest performance (0.96 AUC) using all
379 27,571 open chromatin sites, with decreased performance (0.84 AUC) when using only 2,000
380 sites (**Supplementary Fig. S16D**). Applying Keraon to analyze DFCI Cohort II, we correctly
381 estimated dominant ARPC with undetectable NEPC phenotype in 10 (91%) samples with WGS
382 (mean coverage, 27x) (**Supplementary Fig. 18, Supplementary Table S5**).

383 We performed deeper WGS (22.13x mean coverage, range 15.15x – 31.79x) for the UW Cohort
384 ctDNA samples and applied Keraon to classify the presence of NEPC and to estimate the
385 proportions of ARPC and NEPC phenotypes (**Figure 5H**). Keraon correctly estimated the
386 dominant phenotype (≥ 0.5 relative phenotype fraction) in 25 of 26 (96%) samples with ARPC
387 clinical phenotype and in 5 of 5 (100%) NEPC samples. For 10 samples with presence of ARPC
388 and NEPC phenotypes reported in the clinical histories, Keraon correctly detected both
389 phenotypes in nine samples (NEPC fraction ≥ 0.028 , ARPC fraction ≥ 0.06). In two samples with
390 ARPC-DNPC phenotypes, one was estimated to be ARPC-dominant (0.20 fraction), and in
391 three samples with NEPC-DNPC phenotypes, all three were estimated as being NEPC-
392 dominant (≥ 0.028 fraction). In 14 (82%) out of 17 patients with multiple plasma collected, the
393 predicted phenotypes were consistent across all ctDNA samples. Overall, we observed an
394 accuracy of 97% for correctly classifying ARPC and NEPC dominant phenotypes and 87% for
395 estimating NEPC fractions in samples with admixed clinical phenotypes from ctDNA.

396 **DISCUSSION**

397 The development of minimally invasive blood-based assays of ctDNA to define tumor subtypes
398 has dramatically changed the landscape of clinical oncology. To date, the majority of these
399 assays characterize genomic alterations in oncogenes such as *EGFR* or tumor suppressors,
400 such as *BRCA2*, that inform outlier responses to specific therapeutics. However, tumor
401 classification determined by gene expression analyses, such as the PAM50 subtyping of breast
402 carcinoma and the transcript-based classification of urothelial cancers is also informative of
403 clinical trajectories. Consequently, the ability to characterize tumor phenotype using blood-
404 based assays has the potential to add relevant information for guiding treatment allocation.

405 In the present study, we analyzed multiple features of DNA to infer the activity of gene
406 expression programs corresponding to distinct prostate cancer phenotypes. A key component of

407 the work that allowed for the development of optimized methods and the identification of the
408 most informative ctDNA features was the use of PDX models. The sequencing of mouse plasma
409 provided a unique opportunity to comprehensively interrogate the epigenetic nucleosome
410 patterns in ctDNA from well-characterized tumor models. We developed and applied
411 computational methodologies to evaluate a multitude of ctDNA features, each of which were
412 associated with transcriptional regulation across CRPC tumor phenotypes. The use of PDX
413 mouse plasma overcomes the challenge of low ctDNA content or incomplete knowledge of the
414 tumor when studying patient samples. Using features learned from the PDX ctDNA, we
415 developed models to accurately classify ARPC and NEPC and to estimate their proportions in
416 phenotypically heterogeneous samples from patient plasma in three clinical cohorts. While these
417 data were focused on ARPC and NEPC phenotypes, the approaches may serve as a framework
418 for the use of ctDNA to subtype malignancies arising in other organ sites based on distinctive
419 gene expression programs.

420 The analysis of the LuCaP PDX ctDNA sequencing data confirmed the activity of key regulators
421 between ARPC and NEPC phenotypes, including a set of 47 established differentially
422 expressed genes that associate with cell lineage. While gene expression inference from ctDNA
423 has been shown in proof-of-concept studies (34,41), the PDX ctDNA allowed for a detailed
424 dissection of nucleosome organization associated with transcriptional activity of individual genes
425 that define the tumor phenotypes. Previous analytical approaches have profiled nucleosome
426 occupancy from cfDNA (38,74). However, our assessment of nucleosome stability by means of
427 the Nucleosome Phasing Score is the first to capture the highly variable spacing, positioning,
428 and turnover of the nucleosome arrays associated with transcription and tumor aggressiveness
429 (43,67,68,77).

430 In addition to the existing molecular profiling available for these models, we now provide
431 characterization of histone PTMs in LuCaP PDX tumors using CUT&RUN. At regions with these
432 PTMs on histone tails, we observed expected nucleosome patterns inferred in ctDNA that were
433 consistent with active or repressed gene transcription. To our knowledge, this is the first time
434 that ctDNA analysis has been performed in the context of histone PTMs and will provide a
435 blueprint to develop new approaches for studying additional epigenetic alterations using PDX
436 plasma.

437 While the regulation of key factors such as AR, HOXB13, NKX-3.1, FOXA1, and REST has
438 been shown from ctDNA in CRPC (35,42), we report the differential activity of other key factors

439 in CRPC from ctDNA analysis. This included nuclear factors HNF4G and HNF1A, and
440 pioneering factor GATA2, which are associated with prostate adenocarcinoma (ARPC)
441 (71,73,78). ASCL1 is a pioneer TF with roles in neuronal differentiation and was recently
442 described to be active during NE trans-differentiation and in NEPC (9,55). To our knowledge,
443 this study is the first to demonstrate ASCL1 binding site accessibility and provide a detailed
444 characterization of its transcriptional activity in NEPC from plasma ctDNA.

445 We show an expansive analysis of TFBSs for 338 factors in each plasma sample without the
446 need for chromatin immunoprecipitation or other epigenetic assays. However, we did not find a
447 significant difference in accessibility for 70 out of the 108 TFs in ctDNA, which may be
448 consistent with TF activity not necessarily being correlated with its own expression level (79).
449 On the other hand, the accessibility of TFBSs may not necessarily indicate true TF activity as
450 other co-bound TFs or co-activators/co-repressors influence gene regulation. Moreover, our
451 analyses were based on TFBSs obtained from public databases, including for a limited number
452 of prostate-specific TFs; however, expanded phenotype-specific TF cistrome data may improve
453 this approach.

454 We applied state-of-the-art computational approaches built on existing and new concepts of
455 ctDNA data analysis to extract tumor-specific features, including the representation of
456 nucleosome phasing, periodicity, and spacing associated with transcriptional activity. Other
457 approaches have also considered regions, such as TSSs, TFBSs, and DNase hypersensitivity
458 sites (33,38,41,42); however, after a systematic evaluation, we found that ctDNA features in
459 open chromatin sites derived from ATAC-Seq of PDX tissue (9) provided the highest
460 performance for distinguishing CRPC phenotypes. We presented ctdPheno, which is a
461 probabilistic model that classifies ARPC and NEPC from ULP-WGS data, and Keraon, an
462 analytical model which estimates the proportion of ARPC and NEPC from WGS of patient
463 plasma. Both models are unsupervised and utilize a statistical framework informed directly by
464 parameters from the LuCaP PDX ctDNA analysis. These models do not require training on
465 patient samples but do require tumor fraction estimates (ichorCNA (80)) and in the case of
466 ctdPheno a prediction score cutoff determined from DFCl cohort I. Both frameworks can also be
467 extended to model additional phenotypes. Insights from additional datasets such as single-cell
468 nucleosome and accessibility profiling (81,82) of PDX tumors and clinical samples may improve
469 the resolution for ctDNA analysis. While we observed optimal performance analyzing all open
470 chromatin sites, a smaller subset was still informative which may be useful when considering
471 targeted assays for clinical applications.

472 Applying the prediction models to patient datasets with definitive clinical phenotypes yielded
473 high performance even when using low depth of coverage sequencing. In particular, our
474 performance for the DFCI cohort I was also consistent with the reported phenotype classification
475 results using ctDNA methylation in the same patients (25). Similarly, in the UW cohort, samples
476 with well-defined clinical phenotypes had near-perfect concordance from WGS data. We
477 established the lower limits of phenotype classification performance to be at 8% tumor fraction
478 for ctdPheno (ULP-WGS) and 3% for Keraon (WGS). These results support a strategy whereby
479 ULP-WGS is performed for screening using ctdPheno, along with clinical assessments, and
480 followed-up with standard WGS for more accurate and comprehensive phenotype
481 characterization using Keraon. While this framework may have limited performance for low
482 (<3%) ctDNA levels, it may be optimal at initial assessment of metastatic disease and at tumor
483 progression on therapy, which is when the clinical decision points are most critical.

484 Tumor heterogeneity and co-existence of different molecular phenotypes are common in
485 mCRPC where treatment-induced phenotypic plasticity may vary within and between tumors in
486 an individual patient. In real data simulations and patients with cases of mixed clinical
487 phenotypes, Keraon accurately detected the contributions of mixed phenotypes with a detection
488 limit of 2.8% NEPC, providing the first approach to directly quantify phenotype proportions and
489 heterogeneity from ctDNA. In this study, estimation of phenotype heterogeneity using Keraon
490 required standard depths of WGS. Larger studies with comprehensive assessment of the tumor
491 histologies will be needed for evaluating these models as potential biomarkers of treatment
492 response.

493 In summary, this study illustrates that analysis of ctDNA from PDX mouse plasma at scale can
494 facilitate a detailed investigation of tumor regulation. These results, together with the suite of
495 computational methods presented here, highlight the utility of ctDNA for surveying
496 transcriptional regulation of tumor phenotypes and its potential diagnostic applications in cancer
497 precision medicine.

498 **ACKNOWLEDGEMENTS**

499 We thank the many patients and their families for their altruistic contributions to this study. We
500 thank the Fred Hutchinson Cancer Center Genomics Shared Resources Core members, the
501 Institute for Prostate Cancer Research clinicians and staff that support the University of

502 Washington rapid autopsy program and the PDX program. We thank Patricia Galipeau and
503 members of the Ha and Nelson Laboratories for critically reading this manuscript.

504 **AUTHOR CONTRIBUTIONS**

505 Conceptualization: N.D.S., R.D.P., G.H., P.S.N.

506 Methodology: R.D.P., N.D.S., A-L.D., P.S.N., G.H.

507 Software: R.D.P., A-L.D., N.D.S., B.H., A.J.K., G.H.

508 Formal Analysis: R.D.P., N.D.S., A-L.D., B.H., A.J.K., M.K., M.A., I.M.C., G.H.

509 Investigation: N.D.S., R.D.P., A-L.D., B.H., J.F.S., J.M.L., A.B., G.H.

510 Resources: N.D.S., J.S., S.B., M.P.M., D.H.J., L.S.A., R.F.D., T.A.N., H.M.M., S.C.B., J.E.B.,
511 M.L.F., C.M., H.M.N., E.C., S.H., P.S.N., G.H.

512 Data Curation: N.D.S., R.D.P., A-L.D., M.P.M., S.B., D.H.J., E.C., C.M., A.D.C., M.C.H., P.S.N.,
513 G.H.

514 Writing – Original Draft: R.D.P., N.D.S., P.S.N., G.H.

515 Writing – Review & Editing: N.D.S., R.D.P., A-L.D., C.C.P., C.M., A.D.C., M.T.S., R.B.M., M.C.H.,
516 E.C., K.A., S.H., P.S.N., G.H.

517 Visualization: R.D.P., N.D.S., B.H., M.K., M.C.H., P.S.N., G.H.

518 Supervision: P.S.N., G.H.

519 Funding Acquisition: G.H., P.S.N.

520 MATERIALS AND METHODS

521 *PDX mouse models*

522 The establishment and characterization of the LuCaP PDX models were described previously
523 (83). PDXs were propagated in vivo in male NOD-scid IL2R-gamma-null (NSG) mice
524 (cat#005557). The collection of tumors for the establishment of PDX lines was approved by the
525 University of Washington Human Subjects Division IRB (IRB #2341). PDX lines were evaluated
526 using histopathology by at least two expert pathologists, and histological phenotypic subtype
527 annotations were orthogonally validated based on transcriptome-derived signature marker
528 expression scores to define phenotypes (4,5,22): adenocarcinoma AR-positive (ARPC),
529 neuroendocrine positive (NEPC), and AR-low, neuroendocrine negative (ARLPC). Resected
530 PDX tumors (300-800 mm³) were divided into ~50mg to ~100mg pieces and stored at -80°C.
531 Animal studies were approved by the Fred Hutchinson Cancer Center (FHCC) IACUC (protocol
532 1618) and performed in accordance with the NIH guidelines. For the current study, blood was
533 collected by cardiac puncture from animals bearing PDX tumors (measurable size 300-
534 1400 mm³).

535 *Human subjects*

536 *UW cohort:* Blood samples were collected from men with metastatic castration resistant prostate
537 cancer at the University of Washington (collected under University of Washington Human
538 Subjects Division IRB protocol number CC6932 between years 2014-2021). Patients in this
539 study have provided written informed consent for research participation. In this study, 61 plasma
540 samples from 31 patients were analyzed. After initial ultra-low pass whole genome sequencing
541 (ULP-WGS) analysis, 47 plasma samples from 27 patients with sufficient tumor fraction (> 3%,
542 based on initial ichorCNA analysis using GRCh37 genome build) and three additional samples
543 not meeting the threshold but with clear AR amplification seen in manual curation
544 (FH0243_E_1_A, FH0345_E_1_A, FH0482_E_1_A) were retained for further high depth of
545 coverage whole genome sequencing (WGS) analysis. All samples were de-identified prior to
546 ctDNA analysis and we employed a double blinded approach for evaluating clinical phenotype
547 predictions.

548 *DFCI cohort I:* Plasma was collected from men diagnosed with mCRPC and treated at the
549 Dana-Farber Cancer Institute (DFCI), Brigham and Women's Hospital, or Weill Cornell Medicine
550 (WCM) between April 2003 and August 2021. All patients provided written informed consent for
551 research participation and genomic analysis of their biospecimen and blood. The use of

552 samples was approved by the DFCI IRB (#01-045 and 09-171) and WCM (1305013903) IRBs.
553 The ULP-WGS data at mean coverage 0.5x (range 0.3x – 0.9x) for 101 patients were published
554 previously (25).

555 DFCI cohort II: Plasma samples in this cohort were collected from men diagnosed with mCRPC
556 and treated at the Dana-Farber Cancer Institute (DFCI). All patients provided written informed
557 consent for blood collection and the analysis of their clinical and genetic data for research
558 purposes (DFCI Protocol # 01-045 and 11-104). WGS data at mean coverage 27x (range 11x –
559 44x) (75), and ULP-WGS data at mean coverage 0.13x (range 0.07x – 0.18x) (76,80) were
560 downloaded from dbGAP accession phs001417. Eleven samples from six patients had
561 matching WGS and ULP-WGS with paired-end reads, necessary for analysis by Griffin. Prostate
562 specific antigen (PSA, ng/mL) values and treatment at the time of the blood draw were
563 previously published (76). The six patients were treated for adenocarcinoma using Abiraterone,
564 Enzalutamide, or Bicalutamide, or the patients had detectable levels of PSA.

565 Healthy donor plasma cfDNA WGS data used in this study were obtained from previously
566 published studies. Two samples (HD45 and HD46, both male) with coverage of 13x and 15x,
567 respectively, were accessed from dbGAP under accession phs001417 (75,80). These donors
568 were consented under DFCI protocol IRB (# 03-022). Thirteen healthy donor plasma cfDNA
569 WGS data (12 male: NPH002, 03, 06, 07, 12, 18, 23, 26, 33, 34, 35, 36; 1 female (used in
570 admixtures): NPH004) with coverages between 13.5x – 27.6x were obtained from the European
571 Phenome Archive (EGA) under accession EGAD00001005343 (42).

572 ***PDX plasma processing***

573 Blood samples were collected from NSG mice bearing subcutaneous PDX tumors at the time of
574 sacrifice. The PDX lines were maintained at vivaria in the University of Washington and FHCC.
575 The blood was processed following methods described for human plasma DNA processing for
576 subsequent DNA isolation. Blood was collected in Sarstedt Micro sample tube K3 EDTA tubes
577 and processed within 4 hours. All blood samples were sequentially double spun, first at 2500g
578 for 10 minutes followed by a 16000g centrifugation of the plasma fraction for 10 minutes at room
579 temperature. For each PDX line, 4-8 mouse plasma samples were pooled. Processed plasma
580 samples were preserved in clean, screw-capped cryo-microfuge tubes and stored at -80°C prior
581 to cfDNA isolation.

582 ***Cell-free DNA isolation***

583 The QIAamp Circulating Nucleic Acid Kit was used to isolate cfDNA from PDX mouse-derived
584 plasma using the recommended protocol. The pooled plasma samples from 4-8 mice for each
585 PDX line contained 1.9 to 3 mL total plasma volume for each line. The filter retention-based
586 cfDNA kit method does not implement any fragment size class enrichment. Isolated cfDNA was
587 quantified using the Qubit dsDNA HS assay (Invitrogen) and the cfDNA fragment size profiles
588 were analyzed using TapeStation HS D5000 and HS D1000 assays (Agilent).

589 ***Cell-free DNA library preparation and sequencing***

590 For LuCaP PDX mouse plasma samples, NGS libraries were prepared with 50ng input cfDNA.
591 Illumina NGS sequencing libraries were prepared with the KAPA hyperprep kit, adopting nine
592 cycles of amplification, and purified using lab standardized SPRI beads. We used KAPA UDI
593 dual indexed library adapters. Library concentrations were balanced and pooled for multiplexing
594 and sequenced using the Illumina HiSeq 2500 at the Fred Hutch Genomics Shared Resources
595 (200 cycles) and Illumina NovaSeq platform at the Broad Institute Genomics Platform Walkup-
596 Seq Services using S4 flow cells (300 cycles). To match with Illumina HiSeq 2500 data,
597 truncated 200 cycles FASTQ files were generated (100 bp paired end reads).

598 Clinical patient plasma samples collected at University of Washington (UW cohort) were
599 submitted to the Broad Institute Blood Biopsy Services. Briefly, cfDNA was extracted from 2 mL
600 double-spun plasma and ultra-low-pass whole genome sequencing (ULP-WGS) to
601 approximately 0.2x coverage was performed. The ichorCNA pipeline was used to estimate
602 tumor DNA content (i.e., tumor fraction, see below). Forty-seven samples (from 31 patients) had
603 either $\geq 5\%$ tumor fraction or $\geq 2\%$ tumor fraction with AR amplification observed in ichorCNA
604 and were subsequently sequenced to deeper WGS coverage ($\sim 20x$).

605 ***Cell-free DNA sequencing analysis and mouse subtraction***

606 All cfDNA sequencing data used in this study were realigned to the hg38 (GRCh38) human
607 reference genome (<http://hgdownload.soe.ucsc.edu/goldenPath/hg38/bigZips/hg38.fa.gz>).
608 FASTQ files were realigned using BWA (v0.7.17) mem (84). The complete alignment pipeline
609 including configuration settings may be access at
610 https://github.com/GavinHaLab/fastq_to_bam_paired_snakemake.

611 For PDX ctDNA whole-genome sequence data, we performed mouse genome subtraction
612 following the protocol described previously (85), wherein reads were aligned using BWA mem to

613 a concatenated reference consisting of both human (hg38) and mouse (mm10, GRCm38.p6,
614 [http://igenomes.illumina.com.s3-website-us-east-
615 1.amazonaws.com/Mus_musculus/NCBI/GRCm38/Mus_musculus_NCBI_GRCm38.tar.gz](http://igenomes.illumina.com.s3-website-us-east-1.amazonaws.com/Mus_musculus/NCBI/GRCm38/Mus_musculus_NCBI_GRCm38.tar.gz))
616 reference genomes. Read pairs where both reads aligned to the human reference genome were
617 retained and all other read pairs were removed. Then, remaining reads were re-aligned to the
618 human-only reference. Finally, the GATK best practices workflow was applied to each sample
619 (86); the complete mouse subtraction pipeline used in this study, including tool versions and
620 parameters, can be accessed at https://github.com/GavinHaLab/PDX_mouseSubtraction.
621 Following mouse subtraction samples with < 3X depth were removed for downstream analysis.

622 ***Cell cycle progression (CCP) score calculation***

623 The 31-gene cell cycle proliferation (CCP) signature (68) was computed from RNAseq data
624 using GSVA (87). The single-sample enrichment scores were calculated with default
625 parameters using genome-wide log₂ FPKM values as input for the 31 genes.

626 ***Differential mRNA expression analysis***

627 RNA isolation of 102 tumors from 46 LuCaP PDX samples was performed as described
628 previously (11). RNA concentration, purity, and integrity was assessed by NanoDrop (Thermo
629 Fisher Scientific Inc) and Agilent TapeStation and RNA RIN ≥ 8 was retained for library
630 preparation. RNA-Seq libraries were constructed from 1 ug of total RNA using the Illumina
631 TruSeq Stranded mRNA LT Sample Prep Kit according to the manufacturer's protocol.
632 Barcoded libraries were pooled and sequenced by Illumina NovaSeq 6000 or Illumina HiSeq
633 2500 generating 50 bp paired end reads. Sequencing reads were mapped to the hg38 human
634 reference genome and mm10 mouse reference genomes using STAR.v2.7.3a (88). All
635 subsequent analyses were performed in R-4.1.0. Sequences aligning to the mouse genome and
636 therefor derived from potential contamination with mouse tissue were removed from the analysis
637 using XenofilteR (v1.6) (89). Gene level abundance was quantitated using the R package
638 GenomicAlignments v1.32.0 summarizeOverlaps function using mode=IntersectionStrict,
639 restricted to primary aligned reads. We used refSeq gene annotations for transcriptome analysis.
640 Transcript abundances (FPKM) were input to edgeR v3.38.1 (90), filtered for a minimum
641 expression level using the filterByExpr function with default parameters, and then limma v3.52.1
642 voom was used for differential expression analysis of NEPC vs. ARPC and ARLPC vs. ARPC.
643 We then filtered the results using a list of 1,635 human transcription factors published previously

644 (91), which resulted in 514 genes with $FDR < 0.05$ and \log_2 fold change > 1.58 . Out of these 514,
645 deregulation of gene expression for 404 transcription factor genes delineated ARPC from NEPC.

646 ***Cleavage Under Targets & Release Using Nuclease (CUT&RUN)***

647 CUT&RUN is an antibody targeted enzyme tethering chromatin profiling assay in which
648 controlled cleavage by micrococcal nuclease releases specific protein-DNA complexes into the
649 supernatant for paired-end DNA sequencing analysis. We performed CUT&RUN assays for
650 three histone modifications, H3K27ac, H3K4me1, and H3K27me3, according to published
651 protocols (48). We performed CUT&RUN on LuCaP PDX tumors using ~75mg flash-frozen
652 tissue pieces.

653 Paired-end (50 bp) sequencing was performed and reads were aligned using bowtie2 v2.4.2
654 (92) to the hg38 human reference assembly. Aligned reads were processed as described in the
655 SEACR protocol (<https://github.com/FredHutch/SEACR#preparing-input-bedgraph-files>). Peaks
656 were called using SEACR version 1.3 (49) using “stringent” settings and with reference to paired
657 IgG controls. BigWig files were prepared using bamCoverage in deepTools 3.5.0 (93).
658 Genomewide peak heatmap, targeted heatmap, and respective profiles were plotted using
659 deepTools v3.5.0. bigwig formatted files for each phenotype were obtained using the mean
660 function in wiggletools 1.2.8. and deepTools computeMatrix. Phenotype-specific informative
661 region coordinates were obtained from diffBind v3.5.0, and the top 10,000 most significant
662 regions (all with $FDR < 0.05$) differentially open between ARPC and NEPC lines were used for
663 downstream feature analyses (see Gene body and promoter region selection for additional
664 subsetting criteria applied on a feature-by-feature basis). For heatmaps and profiles the
665 plotHeatmap function was used. We utilized the “Peak Center” option to derive desired
666 heatmaps. These steps were all performed for H3K27ac, H3K4me1 and H3K27me3 antibodies.
667 Scaled heatmap profiles’ area under the curve (AUC; ± 1.5 kbp) and peak height at the profile
668 center were estimated using deepStats v0.4 (<https://zenodo.org/record/3668336>) (comparable
669 profiles are scaled to 10 units).

670 ***Differential histone post-translational modification (PTM) analysis***

671 Differential PTM analysis was performed with the Diffbind version 2.16.0 package (94) in R-
672 4.0.1 using standard parameters
673 (<https://bioconductor.riken.jp/packages/3.0/bioc/html/DiffBind.html>). ARPC, NEPC and ARLPC
674 samples were grouped by histopathological and transcriptome signature defined phenotypes
675 described in the “PDX mouse models” section (**Supplementary Table S2**). Samples were

676 loaded with the dba function, reads counted with the dba.count function, and contrast specified
677 as phenotype with dba.contrast and a minimum members of 2. Differential peak sites were
678 computed with the dba.analyze function with default settings. Differential peak binding of NEPC
679 and ARLPC was computed against ARPC samples. Unique binding sites in NEPC and ARLPC
680 were catalogued using bedtools v2.29.2 (95). Intergroup differentially bound peaks were
681 annotated using ChIPseeker 1.28.3 (96) and TxDb.Hsapiens.UCSC.hg38.knownGene 3.2.2 in
682 R 4.1.0.

683 **ATAC-Seq analysis**

684 ATAC-Seq sequence data for 15 tumor samples from 10 PDX lines were published previously
685 (9). These lines included LuCaP PDX lines with ARPC (23.1, 77, 78, 81, 96) and NEPC (three
686 replicates of 173.1, two replicates each of 49, 93, 145.1, and one replicate of 145.2) phenotypes.
687 Paired end reads were aligned using bowtie2 v2.4.2 (92) to the UCSC hg38 human reference
688 assembly with the "very-sensitive" "-k 10" settings. Peaks were called using Genrich version
689 0.6.1 (<https://github.com/jsh58/Genrich>). Differential binding analysis was performed using
690 Diffbind version 3.5.0 package in R version 4.1.0. ENCODE blacklisted regions were excluded
691 using hg38-blacklist.v2 (97) (<https://github.com/Boyle-Lab/Blacklist>). Phenotype specific regions
692 were isolated by first selecting for positive fold change open chromatin enrichment and then
693 using Intervene 0.6.5 (98) where regions were considered overlapping if they shared at least 1
694 bp with another phenotype. Regions with FDR adjusted p-values < 0.05 were then subset to
695 those overlapping the 3,380,000 established TFBSs (338 TFs x 10,000 binding sites, see Griffin
696 analysis for site selection) by at least 1 bp using BedTools v2.30.0 Intersect. Only regions that
697 overlapped an established TFBS from those lists were retained. For analyses restricted to
698 10,000, 1,000, or 100 sites, sites were ranked and chosen by adjusted p-value.

699 **Nucleosome profiling of ctDNA**

700 Griffin is a method for profiling nucleosome protection and accessibility on predefined genomic
701 loci (51). For this study, Griffin (v0.1.0) was used and can be found on GitHub
702 (<https://github.com/adoebley/Griffin/releases/tag/v0.1.0>). The analysis was performed as
703 follows: First, GC bias was quantified for each sample using an approach described previously
704 (99). Briefly, for each possible fragment length and GC content, the number of reads in a bam
705 file and the number of genomic positions with that specific length and GC content were counted.
706 The GC bias for each fragment length and GC content was calculated by dividing the number of
707 observed reads by the number of observed genomic positions for that fragment length and GC

708 content. The GC bias for all possible GC contents at a given fragment length was then
709 normalized to a mean bias of 1. GC biases were then smoothed by taking the median of values
710 for fragments with similar lengths and GC contents (k nearest neighbors smoothing) to generate
711 smoothed GC bias values.

712 After GC correction, nucleosome profiling was performed in each sample. For each mappable
713 site of interest, fragments aligning to the region \pm 5000 bp from the site were fetched from the
714 bam file. Fragments were filtered to remove duplicates and low-quality alignments (<20
715 mapping quality) and by fragment length. Nucleosome size fragments (140-250 bp) were
716 retained and used in all down-stream Griffin analyses. Fragments were then GC corrected by
717 assigning each fragment a weight of $1/\text{GC_bias}$ for that given fragment length and GC content.
718 The fragment midpoint was identified and the number of weighted fragment midpoints in 15bp
719 bins across the site were counted. For composite sites, all sites of a given type (such as all sites
720 for a given transcription factor) were summed together to generate a single coverage profile.
721 Individual or composite coverage profiles were normalized to a mean coverage of 1 in the \pm
722 5000bp region surrounding the site. Finally, sites were smoothed using a Savitsky-Golay filter
723 with a window length of 165bp and a polynomial order of 3. The window \pm 1000 bp around the
724 site was retained for plotting and feature extraction when plotting sites, shading illustrates the
725 95% confidence interval within sample groups. Features extracted from individual or composite
726 sites included:

- 727 a) “mean central coverage,” the mean coverage between -30 to 30 bp relative to the site
728 center,
- 729 b) “mean window coverage,” the mean coverage between -990 to 990 bp relative to the site
730 center, and
- 731 c) “max wave height,” the absolute difference between the minimum coverage within the
732 window from -120 to 30 bp and maximum coverage in the window from 31 to 195 bp
733 relative to the TSS.

734 ***Transcription factor binding site (TFBS) selection from GTRD***

735 TFBS identified using ChIP-seq were downloaded from the GTRD database version 19.10
736 (https://gtrd.biouml.org/downloads/19.10/chip-seq/Homo%20sapiens_meta_clusters.interval.gz).
737 This database contains binding sites (meta-clusters) that were observed in one or more ChIP
738 seq experiment. Low mappability sites were excluded by examining the mean mappability score
739 in a window around each site (\pm 5000 bp). Mappability information (hg38 Umap multi-read

740 mappability for 50bp reads) was obtained from UCSC genome browser (100)
741 (<https://hgdownload.soe.ucsc.edu/gbdb/hg38/hoffmanMappability/k50.Umap.MultiTrackMappability.bw>). Highly mappable sites (>0.95 mean mappability) were retained for further analysis. 338
742 TFs were selected for analysis using three criteria: (i) TF was contained in GTRD, (ii) had at
743 least 10,000 highly mappable binding sites on autosomes (chr1-22) in GTRD, (iii) TF was
744 present in the CIS-BP database (101) (CIS-BP v2.00 downloaded from
745 <http://cisbp.cabr.utoronto.ca/bulk.php>) and had a known binding motif ('TF_status' is not N).
746 Unless otherwise noted, analyses utilized the top 1,000 TFBSs ranked by the highest
747 'peak.count' across all experiments as computed by GTRD (70). In addition, in the case of AR
748 and ASCL1 we also compared the top 1,000 vs the top 10,000 sites chosen with the same
749 'peak.count' criterion.
750

751 After intersecting these 338 TFs with the 404 differentially expressed TFs identified through
752 RNA-Seq 108 remained. On both the 108 and prostate-specific 41 TFs (described below) we
753 performed unsupervised hierarchical clustering of central window mean values (see Griffin
754 analysis). Hierarchical clustering was performed using the Ward.D2 method with Euclidean
755 distance and complete linkage settings; the groupings were determined using `cutree_cols=2` for
756 columns (LuCaP CRPC phenotypes) and `cutree_rows=13` for rows (TFs) on the dendrograms.

757 To generate a prostate lineage-specific TF set, we first merged GTRD metadata (file;
758 <http://gtrd.biouml.org:8888/downloads/current/metadata/ChIP-seq.metadata.txt> &
759 http://gtrd.biouml.org:8888/downloads/current/metadata/cell_types_and_tissues.metadata.txt).

760 We identified human prostate lineage-specific experiments by restricting the "species" field to
761 "Homo sapiens" and the "title" (tissue or cell type) field by performing a string match of the
762 following {"Prostate", "prostate", "LNCaP", "DU145", "PrEC"}. This resulted in a list of 1,086
763 prostate lineage ChIP seq experiments. Then, we selected metapeaks from the
764 "Homo_sapiens_meta_clusters.interval" file which had been observed in at least one of the
765 prostate lineage experiments using the "exp.set" field. This resulted in a set of 82 TFs. We then
766 filtered the peaks by mappability and kept only highly mappable peaks (as described above).
767 We excluded any TF that wasn't in the initial set of 338 TFs (this removed ChIP targets that
768 weren't true TFs, lacked a known binding site, or didn't have 10,000 total autosomal peaks in
769 GTRD). Of the remaining TFs, we analyzed those with 1,000 highly mappable peaks on
770 autosomes in prostate lineage experiments, resulting in 41 TFs. 20 out of 41 of these TFs
771 overlapped the list of 108 differentially expressed TFs by RNAseq of the PDX tumors. Note that
772 the top 1000 sites for each of the 41 TFs were different than in same TFs of the 338 set

773 because sites must meet the criteria of being derived from at least one experiment involving
774 prostate tissue or cell lines.

775 ***Transcription factor binding site (TFBS) selection from other sources***

776 For AR we further considered 17,619 sites identified through CHIP-seq by Pomerantz et al. (56)
777 (which overlapped 10.9% of the GTRD top 1,000 using bedtools), 41,633 sites identified by
778 Severson et al. (57) across four metastatic tumors (which overlapped 99.4% of the GTRD top
779 1,000). For ASCL1 we obtained 11,124 CHIP-seq sites from Cejas et al. (9) (which overlapped
780 60.9% of the GTRD 1,000). All of these site lists were lifted over from genome build GRCh37 to
781 GRCh38. No mappability filtering was applied so that all possible sites from these prostate
782 experiments and studies were considered.

783 ***Phenotype-lineage specific gene marker selection***

784 We selected 47 genes comprising 12 ARPC and 35 NEPC lineage markers established
785 previously (4,5,58,59) and confirmed by differential expression analysis from PDX tumor RNA-
786 Seq data (**Supplementary Table S3**). In tissues, AR and NE activities were measured on
787 lineage determinant signature gene's mRNA expression (GSVA score)(87). The 47 selected
788 gene list comprises the majority of these signature sets of genes defining mPC characteristic
789 phenotypes or phenotypic activities.

790 ***Gene body and promoter region selection***

791 For individual gene body and promoter analyses Ensembl BioMart v104 (hg38) (102) was used
792 to directly retrieve protein coding transcript start (TSS) and end (TES) coordinates. For promoter
793 region analysis the window ± 1000 bp relative to the TSS was considered. For gene body
794 analysis, the region between the TSS and TES was considered. In the case of genes with
795 multiple transcripts, analyses were limited to the longest transcript resulting in 19,336 regions. In
796 downstream analysis of LuCaP PDX cfDNA, if any lines did not meet specific criteria in a region
797 (including differentially open histone modification regions) that feature/region combination was
798 excluded from analysis, leading to a variable lower number of regions considered based on the
799 feature. These criteria included requiring at least 10 total fragments in a region for all Fragment
800 size analysis (see below) and a non-zero number of "short" and "long" fragments for the short-
801 long ratio; short-long ratios less than 0.01 or greater than 10.0 were also excluded as outliers.
802 For Phasing analysis (see below) we also excluded amplitude components and thus NPS where
803 individual components were 0, or where the ratio was less than 0.01 or greater than 10.0,
804 indicative of insufficient coverage. In the case of mean phased nucleosome distance, if no

805 peaks were identified or the value in a region exceeded 500 (indicative of highly irregular/sparse
806 pileups also from low coverage) those regions were also excluded. Any region with no coverage
807 in a line was excluded from all analyses. This resulted in gene lists that differed in numbers
808 between genomic contexts and feature types.

809 ***Cell-free DNA fragment size analysis***

810 Fragments were first filtered to remove duplicates and low-quality alignments (<20 mapping
811 quality) and by fragment length (15-500 bp). In individual genomic loci/windows, we computed
812 the fragment short-long ratio (FSLR) as the ratio of short (15 - 120 bp) to long (140 - 250 bp)
813 fragments. We also calculated the mean, median absolute deviation (MAD: $median(|X_i -$
814 $median(X)|)$), and coefficient of variation (CV: $\frac{\sigma}{\mu}$ where σ = standard deviation, μ = mean) of the
815 fragment length distribution for each selected window. The fragment size analysis code and
816 implementation used in this study can be accessed at
817 <https://github.com/GavinHaLab/CRPCSubtypingPaper/tree/main/FragmentAnalysis>.

818 ***Nucleosome phasing analysis (TritonNP)***

819 Fragments were first filtered to remove duplicates and low-quality alignments (<20 mapping
820 quality) and by fragment length (nucleosome-sized: 140-250 bp). Next, we performed fragment-
821 level GC bias correction utilizing the same pre-processing method defined in Griffin. A band-
822 pass filter was then applied to the corrected coverage in each region of interest by taking the
823 Fast Fourier Transform (FFT) (scipy.fft v1.8.0) (103) and removing high-frequency components
824 corresponding to frequency components < 146 bp before reconstructing the signal. This cutoff
825 was chosen to ensure that periodic fit signal for downstream evaluation must come from the
826 minimum possible inter-nucleosome distance, thus excluding peak pileups that would not
827 indicate an overall trend in nucleosome phasing. Local peak calling was then done on the
828 smoothed signal to infer average inter nucleosome distance or “phased nucleosome distance”
829 by finding maxima directly. To quantify clarity of overall phasing we took the average frequency
830 amplitude in two bands corresponding to stably bound, well-phased nucleosomes (180-210 bp)
831 and a baseline (150-180 bp), with the former measuring the strength of typically aligned
832 nucleosomes and the latter giving a measure of the underlying signal strength not coming from
833 either high frequency noise or low frequency shifts in total coverage. The ratio of these two
834 amplitude averages forms the Nucleosome Phasing Score (NPS). Because peak locations are
835 assumed to be independent of copy number alterations or depth, and the NPS by virtue of being
836 a ratio divides out any confounding DNA/depth variation between sites, both features are taken

837 as agnostic of CNAs or variable depth. Code and implementation of the method can be found at
838 <https://github.com/denniepatton/TritonNP>.

839 ***ctDNA tumor-normal admixtures and benchmarking***

840 Admixtures for evaluating benchmarking performance were constructed using 5 ARPC (LuCaP
841 35, 35CR, 58, 92, 136CR) and 5 NEPC (LuCaP 49, 93, 145.2, 173.1, 208.4) lines mixed to 1%,
842 5%, 10%, 20%, and 30% tumor fraction with a single healthy donor plasma line (NPH023,
843 EGAD00001005343) for use in binary classification (50 admixes), and in mixtures of 1%, 3%,
844 5%, 10%, 20%, and 30% tumor fraction at ARPC:NEPC ratios, of 0.0, 0.1, 0.3, 0.5, 0.7, 0.9, and
845 1.0 in all possible combinations (810 admixes) for mixture model evaluation. All admixes were
846 mixed at ~25X mean coverage, assuming 100% tumor fraction in post-mouse subtracted PDX
847 sequencing data. After extracting chromosomal DNA (chr1-22, X, Y) with SAMtools v1.14 (104)
848 and removing duplicates with Picard (<https://broadinstitute.github.io/picard/>), SAMtools was
849 used to merge BAM files. To evaluate the ultra-low pass WGS performance, admixtures were
850 then down-sampled using SAMtools to the number of reads corresponding to 1X or 0.2X. During
851 unsupervised benchmarking of each admixture, the healthy donor and the LuCaP line used in
852 the admixture were excluded from the generation of feature distributions to ensure the model
853 would not learn from the lines being interrogated. The admixture pipeline used in this study can
854 be accessed at https://github.com/GavinHaLab/Admixtures_snakemake.

855 ***Supervised binary classification of ARPC and NEPC***

856 Binary classification of ARPC and NEPC subtypes using individual region and feature
857 combinations was conducted using XGBoost v1.4.2 'XGBClassifier' implemented in Python with
858 default parameters. Features included NPS and Mean Phased Nucleosome Distance (see
859 Phasing analysis) in histone modification regions, promoters, and gene bodies; fragment size
860 mean, short-long ratio, and coefficient of variation (see Fragment size analysis) in histone
861 modification regions, promoters, and gene bodies; central and window coverage (see Griffin
862 analysis) in promoters, composite TFBSs, and composite differentially open chromatin regions
863 identified through ATAC-Seq; and Max Wave Height (See Griffin analysis) in promoters. We
864 applied stratified 6-fold cross-validation where two ARPC samples and one NEPC sample were
865 held out in each fold. This was repeated 100 times and performance was computed using area
866 under the receiver operating characteristic (ROC) curve (AUC) and 95% confidence intervals for
867 each individual feature and region combination. Code and implementation of the method can be
868 found at <https://github.com/GavinHaLab/CRPCSubtypingPaper/tree/main/SupervisedLearning>.

869 **Tumor fraction estimation**

870 Tumor fractions from patient plasma samples were assessed using ichorCNA (80) with binSize
871 1,000,000 bp and both GRCh37 and GRCh38 reference genomes. Default tumor fraction
872 estimates reported by ichorCNA were used. See
873 https://github.com/GavinHaLab/CRPCSubtypingPaper/tree/main/ichorCNA_configuration for
874 complete configuration settings.

875 **Phenotype class prediction model (ctdPheno)**

876 We developed a probabilistic model to classify the mCRPC phenotype (ARPC or NEPC) in an
877 individual patient plasma ctDNA sample. This is a generative mixture model that is
878 unsupervised—it does not train on the patient cohort of interest. However, the model accepts
879 the pre-estimated tumor fraction from ichorCNA for the given patient ctDNA sample, as well as
880 the pre-computed ctDNA features values from the LuCaP PDX ctDNA and healthy donor ctDNA
881 as prior information. For each patient ctDNA sample, it fits specific feature values against the
882 pure PDX LuCaP models, shifted towards healthy based on the estimated tumor fraction. The
883 expected feature value (mean μ and standard deviation σ) from each phenotype k for feature i
884 were taken from the mean of LuCaP PDX samples ($\mu_{i,k}$) or taken from the mean of a panel of
885 normals H ($\mu_{i,H}$, male only, $n = 14$; see Healthy Donor cohort). Assuming a Gaussian
886 distribution, feature values were shifted such that the shifted $\mu'_{i,k}$, $\sigma'_{i,k}$ took the form:

$$\mu'_{i,k} = \alpha\mu_{i,k} + (1 - \alpha)\mu_{i,H}$$

$$\sigma'_{i,k} = \sqrt{\alpha\sigma_{i,k}^2 + (1 - \alpha)\sigma_{i,H}^2}$$

887 where α is the tumor fraction estimate for each test sample. In the final model, four features
888 were used: composite open chromatin regions (central and window mean coverage) for specific
889 phenotypes (ARPC and NEPC) identified from the LuCaP PDX ATAC-Seq analysis using Griffin
890 (see Griffin analysis). For each feature i , we then found the probability that the observed sample
891 came from a mixture of the tumor-fraction-corrected Gaussian distributions, where θ is the
892 NEPC mixture weight:

$$p_i(x|\theta) = \theta p(x|k = NEPC) + (1 - \theta)p(x|k = ARPC)$$

893 The θ parameter is estimated by maximizing the joint log-likelihood L for a given patient sample:

$$\theta' = \operatorname{argmax}_{\theta} [L(x|\theta)]$$

$$\text{where } L(x|\theta) = \sum_i \ln[p_i(x|\theta)]$$

894 θ has range [0, 1], where higher values indicate an increased probability of the sample having a
895 NEPC phenotype and was used as the NEPC prediction score metric. Code and implementation
896 of the method can be found at
897 <https://github.com/GavinHaLab/CRPCSubtypingPaper/tree/main/ctdPheno>.

898

899 ***Phenotype heterogeneity prediction and quantification (Keraon)***

900 We developed an analytical model to directly estimate the contributing fractions of ctDNA from
901 different mCRPC phenotypes (ARPC and NEPC) in individual patient plasma ctDNA samples.
902 Like ctdPheno this model is unsupervised and does not require training on the patient cohort of
903 interest. However, the model accepts the pre-estimated tumor fraction from ichorCNA for the
904 given patient ctDNA sample, as well as the pre-computed ctDNA features values from the
905 LuCaP PDX ctDNA and healthy donor ctDNA as prior information (see Class phenotype
906 prediction model).

907

908 As a pre-processing step, the model first computes the mean vector μ_i and covariance matrix Σ_i
909 for each anchor class i in K , under the assumption that each subtype (including healthy) fits a
910 multivariate Gaussian distribution. Based on model constraints, $K - 1$ non-correlated features
911 fully specify the system, and so for ARPC:NEPC:Healthy ($K = 3$) fraction estimation we limited
912 analyses to sets of two features of interest ($F = 2$).

913

914 Next, for each sample defined by some location in feature space \mathbf{v} and estimated tumor fraction
915 t we first performed a change of basis to translate the sample's location from feature space to
916 class space, where each (not necessarily orthogonal) axis defined a single phenotype, and the
917 origin represented pure healthy. If $F = K - 1$, this was accomplished by solving the determined,
918 linear matrix equation for the shifted basis components \mathbf{X} :

$$\mathbf{BX} = \mathbf{S}$$

919 Where $\mathbf{B} = [\mu_{i \neq HD} - \mu_{HD}]$ is the matrix defining all basis vectors from the healthy mean anchor to
920 each phenotype mean anchor, and \mathbf{S} is the vector from the healthy mean anchor to the sample
921 of interest, $\mathbf{S} = \mathbf{v} - \mu_{HD}$. If the system is overdetermined ($F > K - 1$), least squares was used to
922 estimate the approximate solution. This step allows us to learn where in the class space the
923 sample lies, which determined how estimates were evaluated:

- 924 1. Anchor Space: if all basis components are positive then the sample lies within the
 925 volume of order $K - 1$ which has vertices defined by the class means. The relative ratio
 926 of basis component magnitudes in the direction of each class are corrected by estimated
 927 tumor fraction directly: $BC_{i \neq HD} = \frac{X_i}{\sum X} t$
- 928 2. Contra Space: if all basis components are negative then the sample lies within the
 929 volume of order $K - 1$ which forms a reflection of that formed by the class vertices about
 930 healthy. Component fractions for each basis are computed to capture the inverse
 931 distance from the healthy anchor, such that $BC_{i \neq HD} = \frac{X_{i+1}}{\sum(X+1)} t$
- 932 3. Extra Space: if some basis components are positive but others are negative, the sample
 933 lies in some space outside of the anchor or contra space. In this case only positive
 934 contributions are considered, such that $BC_{i \neq HD} = \frac{X_i}{\sum X} t$ for all i such that $X_i > 0$.

935 The tumor fraction normalized basis component estimates BC have range [0,1], where values
 936 directly correspond to the total fraction of each class in the sample.

937 Code and implementation of the method can be found at
 938 <https://github.com/denniepatton/Keraon>.

939

940 ***Analysis and classification of clinical patient samples***

941 After establishing feature distributions using the LuCaP PDX lines and normal panel as
 942 described above, both models were applied to three clinical patient cohorts (see Human
 943 subjects for cohort information).

944 Binary class prediction: Initial scoring using ctdPheno was run on DFCl cohort I, consisting of
 945 101 ULP-WGS samples with paired-end reads. Tumor fraction estimates predicted by ichorCNA
 946 and tumor phenotype classifications were obtained from the original study (25). A prediction
 947 score threshold of 0.3314 for calling NEPC was chosen because it offered an optimal
 948 performance for sensitivity (90%) and specificity (97.5%), where sensitivity is the true positive
 949 rate for identifying NEPC samples $\left(\frac{TP}{TP+FN}\right)$ and specificity is the true negative rate for identifying
 950 ARPC samples $\left(\frac{TN}{TN+FP}\right)$. Alternative thresholds maximizing sensitivity and specificity were
 951 0.1077, at which 95% sensitivity was achieved with a lower specificity of 93.8%, and 0.3769 with
 952 a lower sensitivity of 81.0% but higher specificity of 98.8%. To compare these predictions with
 953 cfDNA methylation (cfMeDIP-seq) classification on the same plasma samples in DFCl cohort I,

954 the concordance was computed between the ctdPheno NEPC prediction score and the cfMeDIP
955 NEPC score obtained from the original study using a 0.15 threshold (25).

956 We then validated the model on two cohorts, beginning with the already published DFCI cohort
957 II (75,76,80). We restricted our analysis to eleven samples from six patients with matched ULP-
958 WGS and WGS data with paired-end reads. Tumor fraction estimates from ichorCNA were
959 obtained from the original study (80). All samples were considered adenocarcinoma (ARPC)
960 based on clinical histories (see Human subjects). The scoring threshold of 0.3314, determined
961 from DFCI cohort I was used for phenotype classification.

962 For the *UW cohort*, consisting of 47 samples from 27 patients (average 22.13X depth of
963 coverage sequencing), ichorCNA was used to estimate sample tumor fractions as described
964 above (GRCh38), while clinical phenotype was determined from clinical histories and expert
965 chart review. We evaluated model performance on matched ULP-WGS and WGS data for
966 unambiguous clinical phenotypes of ARPC and NEPC. The chosen scoring threshold of 0.3314
967 was used, and the fraction of correctly predicted ARPC (n=26) and NEPC (n=5) was computed.
968 The remaining 16 samples with mixed histologies were not evaluated for performance in
969 ctdPheno.

970 Phenotype prediction and proportion estimation: Keraon does not require de novo threshold
971 selection, and so all clinical cohorts were treated as validation sets. Based on the Mean
972 Absolute Error (MAE) of 2.8% for estimating NEPC fraction garnered in the heterogenous
973 mixture benchmarking, this value was chosen as the minimum NEPC fraction threshold for
974 calling presence of NEPC in WGS cohorts. The same tumor fraction estimates used by
975 ctdPheno in ULP were utilized by Keraon, with standard classification conducted on pure clinical
976 phenotypes. The 16 samples with mixed phenotypes in the UW cohort were evaluated both
977 qualitatively and based on the 2.8% threshold in the absence of quantifiable burden estimates
978 from histories.

979 **STATISTICAL ANALYSIS**

980 Quantification of and statistical approaches for high-throughput sequencing data analysis are
981 described in the methods above. When non-parametric distributions (not normally distributed) of
982 numerical values of a particular parameter in a population were compared (using boxplots or in
983 tables), the two-tailed Mann-Whitney U test (also known as the Wilcoxon Rank Sum test;
984 `scipy.stats.mannwhitneyu`, (103) was used to test if any two distributions being compared were

985 significantly different, with Benjamini-Hochberg (statsmodels.stats.multitest.fdr correction,
986 <https://www.statsmodels.org>) correction applied in multiple testing scenarios. All boxplots
987 represent the median with a centerline, interquartile range (IQR) with a box, and first quartile –
988 1.5 IQR and third quartile + 1.5 IQR with whiskers. PCA was conducted in Python
989 (sklearn.decomposition.PCA; <https://scikit-learn.org>)

990 **DATA AVAILABILITY**

991 The LuCaP patient derived xenograft (PDX) plasma ctDNA sequencing data generated in this
992 study can be accessed under NCBI BioProject accession PRJN900550
993 (<https://www.ncbi.nlm.nih.gov/bioproject/PRJNA90055>). The processed patient plasma data can
994 be accessed at <https://github.com/GavinHaLab/CRPCSubtypingPaper/tree/main/Data>. The raw
995 sequencing data generated for the UW cohort are not publicly available because patients did
996 not consent to genomic data sharing but are available upon reasonable request from the
997 corresponding author. This paper also analyzes existing, publicly available data, including
998 LuCaP PDX RNA-Seq (GSE199596) and ATAC-Seq data (GSE156292). The CUT&RUN
999 processed data can be accessed at https://github.com/nielOnav/LuCaP_nucleosome_profile.
1000 Published data for DFCI Cohort I was obtained from the authors (25) after establishing a data
1001 use agreement with the Dana-Farber Cancer Institute.

1002 Any additional information required to reanalyze the data reported in this paper is available from
1003 the lead contact upon request.

1004 **REFERENCES**

- 1005 1. Karantanos T, Corn PG, Thompson TC. Prostate cancer progression after androgen
1006 deprivation therapy: mechanisms of castrate resistance and novel therapeutic approaches.
1007 *Oncogene*. Nature Publishing Group; 2013;32:5501–11.
- 1008 2. Ryan CJ, Smith MR, de Bono JS, Molina A, Logothetis CJ, de Souza P, et al. Abiraterone
1009 in Metastatic Prostate Cancer without Previous Chemotherapy. *N Engl J Med*.
1010 Massachusetts Medical Society; 2013;368:138–48.
- 1011 3. Scher HI, Fizazi K, Saad F, Taplin M-E, Sternberg CN, Miller K, et al. Increased Survival
1012 with Enzalutamide in Prostate Cancer after Chemotherapy. Cabot RC, Harris NL,
1013 Rosenberg ES, Shepard J-AO, Cort AM, Ebeling SH, et al., editors. *New England Journal*
1014 *of Medicine*. 2012;367:1187–97.
- 1015 4. Beltran H, Prandi D, Mosquera JM, Benelli M, Puca L, Cyrta J, et al. Divergent clonal
1016 evolution of castration-resistant neuroendocrine prostate cancer. *Nature Medicine*. Nature
1017 Publishing Group; 2016;22:298–305.
- 1018 5. Bluemn EG, Coleman IM, Lucas JM, Coleman RT, Hernandez-Lopez S, Tharakan R, et al.
1019 Androgen Receptor Pathway-Independent Prostate Cancer Is Sustained through FGF
1020 Signaling. *Cancer cell*. Elsevier; 2017;32:474-489.e6.
- 1021 6. Conteduca V, Oromendia C, Eng KW, Bareja R, Sigouros M, Molina A, et al. Clinical
1022 features of neuroendocrine prostate cancer. *European Journal of Cancer*. 2019;121:7–18.
- 1023 7. Aggarwal R, Huang J, Alumkal JJ, Zhang L, Feng FY, Thomas GV, et al. Clinical and
1024 Genomic Characterization of Treatment-Emergent Small-Cell Neuroendocrine Prostate
1025 Cancer: A Multi-institutional Prospective Study. *JCO*. American Society of Clinical
1026 Oncology; 2018;36:2492–503.
- 1027 8. Baca SC, Takeda DY, Seo J-H, Hwang J, Ku SY, Arafteh R, et al. Reprogramming of the
1028 FOXA1 cistrome in treatment-emergent neuroendocrine prostate cancer. *Nat Commun*.
1029 Nature Publishing Group; 2021;12:1979.
- 1030 9. Cejas P, Xie Y, Font-Tello A, Lim K, Syamala S, Qiu X, et al. Subtype heterogeneity and
1031 epigenetic convergence in neuroendocrine prostate cancer. *Nat Commun*. 2021;12:5775.
- 1032 10. Spetsieris N, Boukovala M, Patsakis G, Alafis I, Efstathiou E. Neuroendocrine and
1033 Aggressive-Variant Prostate Cancer. *Cancers*. Multidisciplinary Digital Publishing Institute;
1034 2020;12:3792.
- 1035 11. Labrecque MP, Coleman IM, Brown LG, True LD, Kollath L, Lakely B, et al. Molecular
1036 profiling stratifies diverse phenotypes of treatment-refractory metastatic castration-resistant
1037 prostate cancer. *J Clin Invest*. American Society for Clinical Investigation; 2019;129:4492–
1038 505.
- 1039 12. Labrecque MP, Alumkal JJ, Coleman IM, Nelson PS, Morrissey C. The heterogeneity of
1040 prostate cancers lacking AR activity will require diverse treatment approaches. *Endocrine-*
1041 *Related Cancer*. Bioscientifica Ltd; 2021;28:T51–66.

- 1042 13. Liu Y, Horn JL, Banda K, Goodman AZ, Lim Y, Jana S, et al. The androgen receptor
1043 regulates a druggable translational regulon in advanced prostate cancer. *Science*
1044 *Translational Medicine*. American Association for the Advancement of Science;
1045 2019;11:eaaw4993.
- 1046 14. Epstein JI, Amin MB, Beltran H, Lotan TL, Mosquera J-M, Reuter VE, et al. Proposed
1047 Morphologic Classification of Prostate Cancer With Neuroendocrine Differentiation. *The*
1048 *American Journal of Surgical Pathology*. 2014;38:756–67.
- 1049 15. Annala M, Taavitsainen S, Khalaf DJ, Vandekerkhove G, Beja K, Sipola J, et al. Evolution
1050 of Castration-Resistant Prostate Cancer in ctDNA during Sequential Androgen Receptor
1051 Pathway Inhibition. *Clinical Cancer Research*. 2021;27:4610–23.
- 1052 16. Aparicio AM, Shen L, Tapia ELN, Lu J-F, Chen H-C, Zhang J, et al. Combined Tumor
1053 Suppressor Defects Characterize Clinically Defined Aggressive Variant Prostate Cancers.
1054 *Clinical Cancer Research*. 2016;22:1520–30.
- 1055 17. Carreira S, Romanel A, Goodall J, Grist E, Ferraldeschi R, Miranda S, et al. Tumor clone
1056 dynamics in lethal prostate cancer. *Science translational medicine*. 2014;6:254ra125.
- 1057 18. Du M, Tian Y, Tan W, Wang L, Wang L, Kilari D, et al. Plasma cell-free DNA-based
1058 predictors of response to abiraterone acetate/prednisone and prognostic factors in
1059 metastatic castration-resistant prostate cancer. *Prostate Cancer Prostatic Dis*. Nature
1060 Publishing Group; 2020;23:705–13.
- 1061 19. Sumanasuriya S, Seed G, Parr H, Christova R, Pope L, Bertan C, et al. Elucidating
1062 Prostate Cancer Behaviour During Treatment via Low-pass Whole-genome Sequencing of
1063 Circulating Tumour DNA. *European Urology*. 2021;80:243–53.
- 1064 20. Ulz P, Belic J, Graf R, Auer M, Lafer I, Fischereder K, et al. Whole-genome plasma
1065 sequencing reveals focal amplifications as a driving force in metastatic prostate cancer.
1066 *Nat Commun*. Institute of Human Genetics, Medical University of Graz, A-8010 Graz,
1067 Austria. Department of Urology, Medical University of Graz, A-8036 Graz, Austria.
1068 Department of Internal Medicine I, Hospital Barmherzige Schwestern Linz, A-4020 Linz,
1069 Austria. *Departme*; 2016;7:12008.
- 1070 21. Wyatt AW, Annala M, Aggarwal R, Beja K, Feng F, Youngren J, et al. Concordance of
1071 Circulating Tumor DNA and Matched Metastatic Tissue Biopsy in Prostate Cancer. *JNCI:*
1072 *Journal of the National Cancer Institute*. Oxford University Press; 2018;110:78–86.
- 1073 22. Nyquist MD, Corella A, Coleman I, De Sarkar N, Kaipainen A, Ha G, et al. Combined TP53
1074 and RB1 Loss Promotes Prostate Cancer Resistance to a Spectrum of Therapeutics and
1075 Confers Vulnerability to Replication Stress. *Cell Reports*. 2020;31:107669.
- 1076 23. Berger A, Brady NJ, Bareja R, Robinson B, Conteduca V, Augello MA, et al. N-Myc–
1077 mediated epigenetic reprogramming drives lineage plasticity in advanced prostate cancer.
1078 *J Clin Invest*. American Society for Clinical Investigation; 2019;129:3924–40.
- 1079 24. Beltran H, Romanel A, Conteduca V, Casiraghi N, Sigouros M, Franceschini GM, et al.
1080 Circulating tumor DNA profile recognizes transformation to castration-resistant

- 1081 neuroendocrine prostate cancer. *J Clin Invest*. American Society for Clinical Investigation;
1082 2020;130:1653–68.
- 1083 25. Berchuck JE, Baca SC, McClure HM, Korthauer K, Tsai HK, Nuzzo PV, et al. Detecting
1084 Neuroendocrine Prostate Cancer Through Tissue-Informed Cell-Free DNA Methylation
1085 Analysis. *Clinical Cancer Research*. 2022;28:928–38.
- 1086 26. Shen SY, Singhanian R, Fehringer G, Chakravarthy A, Roehrl MHA, Chadwick D, et al.
1087 Sensitive tumour detection and classification using plasma cell-free DNA methylomes.
1088 *Nature*. Nature Publishing Group; 2018;563:579–83.
- 1089 27. Wu A, Cremaschi P, Wetterskog D, Conteduca V, Franceschini GM, Kleftogiannis D, et al.
1090 Genome-wide plasma DNA methylation features of metastatic prostate cancer. *J Clin
1091 Invest*. American Society for Clinical Investigation; 2020;130:1991–2000.
- 1092 28. Heitzer E, Aunger L, Speicher MR. Cell-Free DNA and Apoptosis: How Dead Cells Inform
1093 About the Living. *Trends in Molecular Medicine*. Elsevier Ltd; 2020;26:519–28.
- 1094 29. Lo YMD, Han DSC, Jiang P, Chiu RWK. Epigenetics, fragmentomics, and topology of cell-
1095 free DNA in liquid biopsies. *Science [Internet]*. American Association for the Advancement
1096 of Science; 2021 [cited 2021 Apr 12];372. Available from:
1097 <https://science.sciencemag.org/content/372/6538/eaaw3616>
- 1098 30. Cristiano S, Leal A, Phallen J, Fiksel J, Adleff V, Bruhm DC, et al. Genome-wide cell-free
1099 DNA fragmentation in patients with cancer. *Nature*. Nature Publishing Group;
1100 2019;570:385–9.
- 1101 31. Jiang P, Sun K, Peng W, Cheng SH, Ni M, Yeung PC, et al. Plasma DNA End-Motif
1102 Profiling as a Fragmentomic Marker in Cancer, Pregnancy, and Transplantation. *Cancer
1103 Discov*. American Association for Cancer Research; 2020;10:664–73.
- 1104 32. Mathios D, Johansen JS, Cristiano S, Medina JE, Phallen J, Larsen KR, et al. Detection
1105 and characterization of lung cancer using cell-free DNA fragmentomes. *Nat Commun*.
1106 2021;12:5060.
- 1107 33. Peneder P, Stütz AM, Surdez D, Krumbholz M, Semper S, Chicard M, et al. Multimodal
1108 analysis of cell-free DNA whole-genome sequencing for pediatric cancers with low
1109 mutational burden. *Nat Commun*. Nature Publishing Group; 2021;12:3230.
- 1110 34. Zhu G, Guo YA, Ho D, Poon P, Poh ZW, Wong PM, et al. Tissue-specific cell-free DNA
1111 degradation quantifies circulating tumor DNA burden. *Nature Communications*. Nature
1112 Publishing Group; 2021;12:2229.
- 1113 35. Herberts C, Annala M, Sipola J, Ng SWS, Chen XE, Nurminen A, et al. Deep whole-
1114 genome ctDNA chronology of treatment-resistant prostate cancer. *Nature*. 2022;608:199–
1115 208.
- 1116 36. Jiang P, Chan CWM, Chan KCA, Cheng SH, Wong J, Wong VW-S, et al. Lengthening and
1117 shortening of plasma DNA in hepatocellular carcinoma patients. *Proceedings of the
1118 National Academy of Sciences of the United States of America*. 2015;112:E1317-25.

- 1119 37. Mouliere F, Chandrananda D, Piskorz AM, Moore EK, Morris J, Ahlborn LB, et al.
1120 Enhanced detection of circulating tumor DNA by fragment size analysis. *Science*
1121 *Translational Medicine*. 2018;10:eaat4921.
- 1122 38. Snyder MW, Kircher M, Hill AJ, Daza RM, Shendure J. Cell-free DNA Comprises an in
1123 Vivo Nucleosome Footprint that Informs Its Tissues-Of-Origin. *Cell*. Elsevier Inc.;
1124 2016;164:57–68.
- 1125 39. Underhill HR, Kitzman JO, Hellwig S, Welker NC, Daza R, Baker DN, et al. Fragment
1126 Length of Circulating Tumor DNA. *PLOS Genet*. 2016;12:426–37.
- 1127 40. Ramachandran S, Ahmad K, Henikoff S. Transcription and Remodeling Produce
1128 Asymmetrically Unwrapped Nucleosomal Intermediates. *Molecular Cell*. Cell Press;
1129 2017;68:1038-1053.e4.
- 1130 41. Ulz P, Thallinger GG, Auer M, Graf R, Kashofer K, Jahn SW, et al. Inferring expressed
1131 genes by whole-genome sequencing of plasma DNA. *Nature Genetics*. Nature Publishing
1132 Group; 2016;48:1273–8.
- 1133 42. Ulz P, Perakis S, Zhou Q, Moser T, Belic J, Lazzeri I, et al. Inference of transcription factor
1134 binding from cell-free DNA enables tumor subtype prediction and early detection. *Nature*
1135 *Communications*. 2019;10:4666.
- 1136 43. Brahma S, Henikoff S. Epigenome Regulation by Dynamic Nucleosome Unwrapping.
1137 *Trends in Biochemical Sciences*. Elsevier; 2020;45:13–26.
- 1138 44. Lai WKM, Pugh BF. Understanding nucleosome dynamics and their links to gene
1139 expression and DNA replication. *Nat Rev Mol Cell Biol*. 2017;18:548–62.
- 1140 45. Yen K, Vinayachandran V, Batta K, Koerber RT, Pugh BF. Genome-wide Nucleosome
1141 Specificity and Directionality of Chromatin Remodelers. *Cell*. 2012;149:1461–73.
- 1142 46. Rao S, Han AL, Zukowski A, Kopin E, Sartorius CA, Kabos P, et al. Transcription factor–
1143 nucleosome dynamics from plasma cfDNA identifies ER-driven states in breast cancer.
1144 *Science Advances*. American Association for the Advancement of Science;
1145 2022;8:eabm4358.
- 1146 47. Nguyen HM, Vessella RL, Morrissey C, Brown LG, Coleman IM, Higano CS, et al. LuCaP
1147 Prostate Cancer Patient-Derived Xenografts Reflect the Molecular Heterogeneity of
1148 Advanced Disease and Serve as Models for Evaluating Cancer Therapeutics. *The*
1149 *Prostate*. John Wiley & Sons, Ltd; 2017;77:654–71.
- 1150 48. Skene PJ, Henikoff S. An efficient targeted nuclease strategy for high-resolution mapping
1151 of DNA binding sites. Reinberg D, editor. *eLife*. eLife Sciences Publications, Ltd;
1152 2017;6:e21856.
- 1153 49. Meers MP, Tenenbaum D, Henikoff S. Peak calling by Sparse Enrichment Analysis for
1154 CUT&RUN chromatin profiling. *Epigenetics & Chromatin*. 2019;12:42.
- 1155 50. Zhou VW, Goren A, Bernstein BE. Charting histone modifications and the functional
1156 organization of mammalian genomes. *Nat Rev Genet*. 2011;12:7–18.

- 1157 51. Doebley A-L, Ko M, Liao H, Cruikshank AE, Kikawa C, Santos K, et al. Griffin: Framework
1158 for clinical cancer subtyping from nucleosome profiling of cell-free DNA. medRxiv.
1159 2021;2021.08.31.21262867.
- 1160 52. Soares LM, He PC, Chun Y, Suh H, Kim T, Buratowski S. Determinants of Histone H3K4
1161 Methylation Patterns. *Molecular Cell*. 2017;68:773-785.e6.
- 1162 53. Brady NJ, Bagadion AM, Singh R, Conteduca V, Van Emmenis L, Arceci E, et al. Temporal
1163 evolution of cellular heterogeneity during the progression to advanced AR-negative
1164 prostate cancer. *Nat Commun*. Nature Publishing Group; 2021;12:3372.
- 1165 54. Wang YA, Sfakianos J, Tewari AK, Cordon-cardo C, Kyprianou N. Molecular tracing of
1166 prostate cancer lethality. *Oncogene*. Nature Publishing Group; 2020;39:7225–38.
- 1167 55. Rapa I, Ceppi P, Bollito E, Rosas R, Cappia S, Bacillo E, et al. Human ASH1 expression in
1168 prostate cancer with neuroendocrine differentiation. *Mod Pathol*. Nature Publishing Group;
1169 2008;21:700–7.
- 1170 56. Pomerantz MM, Qiu X, Zhu Y, Takeda DY, Pan W, Baca SC, et al. Prostate cancer
1171 reactivates developmental epigenomic programs during metastatic progression. *Nat Genet*.
1172 2020;52:790–9.
- 1173 57. Severson TM, Zhu Y, De Marzo AM, Jones T, Simons JW, Nelson WG, et al. Epigenetic
1174 and transcriptional analysis reveals a core transcriptional program conserved in clonal
1175 prostate cancer metastases. *Molecular Oncology*. 2021;15:1942–55.
- 1176 58. Labrecque MP, Brown LG, Coleman IM, Lakely B, Brady NJ, Lee JK, et al. RNA Splicing
1177 Factors SRRM3 and SRRM4 Distinguish Molecular Phenotypes of Castration-Resistant
1178 Neuroendocrine Prostate Cancer. *Cancer Research*. 2021;81:4736–50.
- 1179 59. Tsai HK, Lehrer J, Alshalalfa M, Erho N, Davicioni E, Lotan TL. Gene expression
1180 signatures of neuroendocrine prostate cancer and primary small cell prostatic carcinoma.
1181 *BMC Cancer*. 2017;17:759.
- 1182 60. Jiang Z, Zhang B. On the role of transcription in positioning nucleosomes. *PLOS*
1183 *Computational Biology*. Public Library of Science; 2021;17:e1008556.
- 1184 61. Klemm SL, Shipony Z, Greenleaf WJ. Chromatin accessibility and the regulatory
1185 epigenome. *Nature Reviews Genetics*. Nature Publishing Group; 2019;20:207–20.
- 1186 62. Oruba A, Sacconi S, van Essen D. Role of cell-type specific nucleosome positioning in
1187 inducible activation of mammalian promoters. *Nat Commun*. 2020;11:1075.
- 1188 63. Guo Y, Zhao S, Wang GG. Polycomb Gene Silencing Mechanisms: PRC2 Chromatin
1189 Targeting, H3K27me3 “Readout”, and Phase Separation-Based Compaction. *Trends in*
1190 *Genetics*. Elsevier; 2021;37:547–65.
- 1191 64. Jiang C, Pugh BF. Nucleosome positioning and gene regulation: advances through
1192 genomics. *Nat Rev Genet*. 2009;10:161–72.

- 1193 65. Saxton DS, Rine J. Nucleosome Positioning Regulates the Establishment, Stability, and
1194 Inheritance of Heterochromatin in *Saccharomyces cerevisiae*. *Proceedings of the National*
1195 *Academy of Sciences*. *Proceedings of the National Academy of Sciences*;
1196 2020;117:27493–501.
- 1197 66. Valouev A, Johnson SM, Boyd SD, Smith CL, Fire AZ, Sidow A. Determinants of
1198 nucleosome organization in primary human cells. *Nature*. Nature Publishing Group;
1199 2011;474:516–20.
- 1200 67. Deal RB, Henikoff JG, Henikoff S. Genome-Wide Kinetics of Nucleosome Turnover
1201 Determined by Metabolic Labeling of Histones. *Science*. American Association for the
1202 *Advancement of Science*; 2010;328:1161–4.
- 1203 68. Cuzick J, Swanson GP, Fisher G, Brothman AR, Berney DM, Reid JE, et al. Prognostic
1204 value of an RNA expression signature derived from cell cycle proliferation genes in
1205 patients with prostate cancer: a retrospective study. *The Lancet Oncology*. 2011;12:245–
1206 55.
- 1207 69. Chereji RV, Bryson TD, Henikoff S. Quantitative MNase-seq accurately maps nucleosome
1208 occupancy levels. *Genome Biology*. 2019;20:198.
- 1209 70. Yevshin I, Sharipov R, Kolmykov S, Kondrakhin Y, Kolpakov F. GTRD: a database on
1210 gene transcription regulation—2019 update. *Nucleic Acids Res*. Oxford Academic;
1211 2019;47:D100–5.
- 1212 71. Arora VK, Schenkein E, Murali R, Subudhi SK, Wongvipat J, Balbas MD, et al.
1213 Glucocorticoid Receptor Confers Resistance to Antiandrogens by Bypassing Androgen
1214 Receptor Blockade. *Cell*. Elsevier; 2013;155:1309–22.
- 1215 72. Mu P, Zhang Z, Benelli M, Karthaus WR, Hoover E, Chen C-C, et al. SOX2 promotes
1216 lineage plasticity and antiandrogen resistance in TP53- and RB1-deficient prostate cancer.
1217 *Science*. American Association for the Advancement of Science; 2017;355:84–8.
- 1218 73. Shukla S, Cyrtá J, Murphy DA, Walczak EG, Ran L, Agrawal P, et al. Aberrant Activation of
1219 a Gastrointestinal Transcriptional Circuit in Prostate Cancer Mediates Castration
1220 Resistance. *Cancer Cell*. Elsevier; 2017;32:792-806.e7.
- 1221 74. Sun K, Jiang P, Cheng SH, Cheng THT, Wong J, Wong VWS, et al. Orientation-aware
1222 plasma cell-free DNA fragmentation analysis in open chromatin regions informs tissue of
1223 origin. *Genome research*. Cold Spring Harbor Laboratory Press; 2019;29:418–27.
- 1224 75. Viswanathan SR, Ha G, Hoff AM, Wala JA, Carrot-Zhang J, Whelan CW, et al. Structural
1225 Alterations Driving Castration-Resistant Prostate Cancer Revealed by Linked-Read
1226 Genome Sequencing. *Cell*. Elsevier; 2018;174:433-447.e19.
- 1227 76. Choudhury AD, Werner L, Francini E, Wei XX, Ha G, Freeman SS, et al. Tumor fraction in
1228 cell-free DNA as a biomarker in prostate cancer. *JCI Insight* [Internet]. American Society
1229 for Clinical Investigation; 2018 [cited 2019 Mar 1];3. Available from:
1230 <https://insight.jci.org/articles/view/122109>

- 1231 77. Klein DC, Hainer SJ. Genomic methods in profiling DNA accessibility and factor
1232 localization. *Chromosome Res.* 2020;28:69–85.
- 1233 78. Chaytor L, Simcock M, Nakjang S, Heath R, Walker L, Robson C, et al. The Pioneering
1234 Role of GATA2 in Androgen Receptor Variant Regulation Is Controlled by Bromodomain
1235 and Extraterminal Proteins in Castrate-Resistant Prostate Cancer. *Mol Cancer Res.*
1236 American Association for Cancer Research; 2019;17:1264–78.
- 1237 79. Corces MR, Granja JM, Shams S, Louie BH, Seoane JA, Zhou W, et al. The chromatin
1238 accessibility landscape of primary human cancers. *Science.* 2018;362.
- 1239 80. Adalsteinsson VA, Ha G, Freeman SS, Choudhury AD, Stover DG, Parsons HA, et al.
1240 Scalable whole-exome sequencing of cell-free DNA reveals high concordance with
1241 metastatic tumors. *Nature Communications.* 2017;8.
- 1242 81. Fang R, Preissl S, Li Y, Hou X, Lucero J, Wang X, et al. Comprehensive analysis of single
1243 cell ATAC-seq data with SnapATAC. *Nat Commun.* Nature Publishing Group;
1244 2021;12:1337.
- 1245 82. Wu SJ, Furlan SN, Mihalas AB, Kaya-Okur HS, Feroze AH, Emerson SN, et al. Single-cell
1246 CUT&Tag analysis of chromatin modifications in differentiation and tumor progression. *Nat*
1247 *Biotechnol.* 2021;39:819–24.
- 1248 83. Lam H-M, Nguyen HM, Corey E. Generation of Prostate Cancer Patient-Derived
1249 Xenografts to Investigate Mechanisms of Novel Treatments and Treatment Resistance. In:
1250 Culig Z, editor. *Prostate Cancer: Methods and Protocols* [Internet]. New York, NY:
1251 Springer; 2018 [cited 2022 Mar 22]. page 1–27. Available from:
1252 https://doi.org/10.1007/978-1-4939-7845-8_1
- 1253 84. Li H. Aligning sequence reads, clone sequences and assembly contigs with BWA-MEM.
1254 arXiv:13033997 [q-bio] [Internet]. 2013 [cited 2022 Mar 22]; Available from:
1255 <http://arxiv.org/abs/1303.3997>
- 1256 85. Jo S-Y, Kim E, Kim S. Impact of mouse contamination in genomic profiling of patient-
1257 derived models and best practice for robust analysis. *Genome Biology.* 2019;20:231.
- 1258 86. DePristo MA, Banks E, Poplin R, Garimella KV, Maguire JR, Hartl C, et al. A framework for
1259 variation discovery and genotyping using next-generation DNA sequencing data. *Nat*
1260 *Genet.* Nature Publishing Group; 2011;43:491–8.
- 1261 87. Hänzelmann S, Castelo R, Guinney J. GSEA: gene set variation analysis for microarray
1262 and RNA-Seq data. *BMC Bioinformatics.* 2013;14:7.
- 1263 88. Dobin A, Davis CA, Schlesinger F, Drenkow J, Zaleski C, Jha S, et al. STAR: ultrafast
1264 universal RNA-seq aligner. *Bioinformatics.* 2013;29:15–21.
- 1265 89. Kluin RJC, Kemper K, Kuilman T, de Ruyter JR, Iyer V, Forment JV, et al. Xenofilter:
1266 computational deconvolution of mouse and human reads in tumor xenograft sequence
1267 data. *BMC Bioinformatics.* 2018;19:366.

- 1268 90. Robinson MD, McCarthy DJ, Smyth GK. edgeR: a Bioconductor package for differential
1269 expression analysis of digital gene expression data. *Bioinformatics*. 2010;26:139–40.
- 1270 91. Lambert SA, Jolma A, Campitelli LF, Das PK, Yin Y, Albu M, et al. The Human
1271 Transcription Factors. *Cell*. 2018;172:650–65.
- 1272 92. Langmead B, Wilks C, Antonescu V, Charles R. Scaling read aligners to hundreds of
1273 threads on general-purpose processors. *Bioinformatics*. 2019;35:421–32.
- 1274 93. Ramírez F, Ryan DP, Grüning B, Bhardwaj V, Kilpert F, Richter AS, et al. deepTools2: a
1275 next generation web server for deep-sequencing data analysis. *Nucleic Acids Research*.
1276 2016;44:W160–5.
- 1277 94. Ross-Innes CS, Stark R, Teschendorff AE, Holmes KA, Ali HR, Dunning MJ, et al.
1278 Differential oestrogen receptor binding is associated with clinical outcome in breast cancer.
1279 *Nature*. 2012;481:389–93.
- 1280 95. Quinlan AR, Hall IM. BEDTools: a flexible suite of utilities for comparing genomic features.
1281 *Bioinformatics*. 2010;26:841–2.
- 1282 96. Yu G, Wang L-G, He Q-Y. ChIPseeker: an R/Bioconductor package for ChIP peak
1283 annotation, comparison and visualization. *Bioinformatics*. 2015;31:2382–3.
- 1284 97. Amemiya HM, Kundaje A, Boyle AP. The ENCODE Blacklist: Identification of Problematic
1285 Regions of the Genome. *Sci Rep*. Nature Publishing Group; 2019;9:9354.
- 1286 98. Khan A, Mathelier A. Intervene: a tool for intersection and visualization of multiple gene or
1287 genomic region sets. *BMC Bioinformatics*. 2017;18:287.
- 1288 99. Benjamini Y, Speed TP. Summarizing and correcting the GC content bias in high-
1289 throughput sequencing. *Nucleic Acids Research*. 2012;40:e72–e72.
- 1290 100. Karimzadeh M, Ernst C, Kundaje A, Hoffman MM. Umap and Bimap: quantifying genome
1291 and methylome mappability. *Nucleic Acids Research*. 2018;46:e120.
- 1292 101. Weirauch MT, Yang A, Albu M, Cote AG, Montenegro-Montero A, Drewe P, et al.
1293 Determination and inference of eukaryotic transcription factor sequence specificity. *Cell*.
1294 2014;158:1431–43.
- 1295 102. Howe KL, Achuthan P, Allen J, Allen J, Alvarez-Jarreta J, Amode MR, et al. Ensembl 2021.
1296 *Nucleic Acids Research*. 2021;49:D884–91.
- 1297 103. Virtanen P, Gommers R, Oliphant TE, Haberland M, Reddy T, Cournapeau D, et al. SciPy
1298 1.0: fundamental algorithms for scientific computing in Python. *Nat Methods*. Nature
1299 Publishing Group; 2020;17:261–72.
- 1300 104. Danecek P, Bonfield JK, Liddle J, Marshall J, Ohan V, Pollard MO, et al. Twelve years of
1301 SAMtools and BCftools. *GigaScience*. 2021;10:giab008.

1302 **Figure 1. Characterizing advanced prostate cancer through matched tumor and liquid**
1303 **biopsies from PDX models**

1304 **(A) (top)** Both blood and tissue samples were taken from 26 patient-derived xenograft
1305 (PDX) mouse models with tumors originating from metastatic castration-resistant
1306 prostate cancer (mCRPC) with AR-positive adenocarcinoma (ARPC), neuroendocrine
1307 (NEPC), AR-low neuroendocrine-negative (ARLPC) phenotypes. Cell-free DNA (cfDNA)
1308 was extracted from pooled plasma collected from 4-8 mice and whole genome
1309 sequencing (WGS) was performed. Following bioinformatic mouse read subtraction,
1310 pure human circulating tumor DNA (ctDNA) reads remained. From PDX tissue, ATAC-
1311 Seq and CUT&RUN (targeting H3K27ac, H3K4me1, and H3K27me3) data were
1312 generated. **(middle)** Four distinct ctDNA features were analyzed at five genomic region
1313 types using Griffin (51) or nucleosome phasing methods developed in this study
1314 **(Methods)**. **(bottom, left)** Overview of PDX ctDNA features profiled to characterize the
1315 mCRPC pathways, transcriptional regulation, and nucleosome positioning. ctDNA
1316 features were evaluated for phenotype classification. **(bottom, right)** Phenotype
1317 classification using probabilistic and analytical models that accounted for ctDNA tumor
1318 content and were informed by PDX features were applied to 159 samples in three
1319 patient cohorts.

1320 **(B)** PDX phenotypes and mouse plasma sequencing. Inclusion status based on final mean
1321 depth after mouse read subtraction ($< 3x$ coverage were excluded; red dotted line).
1322 Phenotype status, including 6 NEPC, 18 ARPC (2 excluded), and 2 ARLPC. Average
1323 depth of coverage before and after mouse subtraction (mean coverage 20.5x; dotted
1324 line). Percentage of the cfDNA sample that contains human ctDNA after mouse read
1325 subtraction.

1326

1327 **Figure 2. Analysis of tumor histone modifications and ctDNA reveals nucleosome**
1328 **patterns consistent with transcriptional regulation in CRPC phenotype-specific genes**

1329 **(A)** H3K27ac peak signals between ARLPC, ARPC, and NEPC PDX tumor phenotypes at
1330 10,000 AR binding sites (left) and at ASCL1 binding sites (right). Binding sites were
1331 selected from the GTRD (70) (**Methods**).

1332 **(B-C)** Composite coverage profiles at 1,000 AR **(B)** and ASCL1 **(C)** binding sites in ctDNA
1333 analyzed using Griffin for 140-250 bp fragments (Methods). Coverage profile means
1334 (lines) and 95% confidence interval computed using 1000 bootstraps for a subset of
1335 sites (shading) are shown. The region ± 150 bp is indicated with vertical dotted line and
1336 yellow shading.

1337 **(D)** Heatmap of \log_2 fold change in 47 key genes up and down regulated between ARPC
1338 and NEPC established through RNA-Seq **(left)** grouped by the type of histone
1339 modification which dictates translation levels: Group 1 shows genes activity attributable
1340 to H3K27ac or H3K4me1 PTM marks in the gene promoters or putative distal enhancers
1341 and lacking H3K27me3 heterochromatic mark in the gene body; Group 2 features gene
1342 body spanning H3K27me3 repression marks. Central columns show differential peak
1343 intensity for each of the assayed histone modifications, separated by whether they
1344 appear upstream or in the promoter or the body of each gene. On the right the \log_2 fold
1345 change between ARPC and NEPC lines' cfDNA fragment size coefficient of variation
1346 (CV) is shown for TSS \pm 1KB windows and respective gene bodies.

1347 **(E)** Comparison of the \log_2 fold change (ARPC/NEPC) of mean mRNA expression vs mean
1348 coefficient of variation (CV) in the 47 phenotypic lineage marker genes' promoter regions.

1349 **(F) (top)** Illustrations of expected ctDNA coverage profiles for Group 1 genes with and
1350 without H3K27ac or H3K4me1 modification leading to active and inactive transcription,
1351 respectively. **(bottom)** ± 1000 bp surrounding the promoter region for AR and ASCL1 in
1352 ARPC and NEPC. Shown are coverage profile means (lines) and 95% confidence
1353 interval computed using 1000 bootstraps for a subset of sites (shading). Decreased
1354 coverage is reflective of increased nucleosome accessibility and thus increased
1355 transcription. Dotted line and yellow shading highlight the transcription start site (TSS) at
1356 -230 bp and $+170$ bp.

1357 **(G)** Illustration of expected ctDNA coverage profiles for Group 2 genes with repressed
1358 transcription caused by H3K27me3 modifications in the gene body. Neuronal gene
1359 UNC13A has increased nucleosome phasing in ctDNA of ARPC samples compared to
1360 NEPC.

1361 **Figure 3. Phasing analysis in ctDNA recapitulates nucleosome stability and trends in**
1362 **transcriptional activity between CRPC phenotypes**

- 1363 (A) Illustration of nucleosome phasing analysis using TritonNP for HOXB13, which is
1364 expressed in ARPC but not NEPC. Fourier transform and a band-pass filter-based
1365 smoothing method was used to identify phased peaks (grey dotted lines). Frequency
1366 components corresponding to nucleosome dyads (wavelength > 146 bp) are shown in
1367 purple. The mean inter-nucleosome distance was computed from all peaks in the gene
1368 body: lower values represent more periodic and stable nucleosomes. Nucleosome
1369 Phasing Score (NPS) is defined as the ratio of the mean amplitudes between frequency
1370 components 180-210 bp (“stable”, green curve) and 150-180 bp (“baseline”, red curve).
- 1371 (B) Boxplot of mean phased-nucleosome distance in 17,946 gene bodies per ctDNA sample
1372 for ARPC and NEPC PDX lines. Two-tailed Mann-Whitney U test p-value shown.
- 1373 (C) Comparison of the mean phased-nucleosome distance and the mean cell-cycle
1374 progression (CCP) score (estimated from RNA-Seq) for 16 ARPC and 6 NEPC PDX
1375 lines.
- 1376 (D) Boxplot of NPS in gene bodies of 47 phenotype-defining genes (35 NE-regulated and 12
1377 AR-regulated) between ARPC and NEPC lines. Two-tailed Mann-Whitney U test p-
1378 values shown.
- 1379 (E) Volcano plot of NPS log₂-fold-change (ARPC/NEPC) in the 47 phenotype-defining genes.
1380 Genes with significantly higher NPS scores (solid-colored dots (two-tailed Mann-Whitney
1381 U test, Benjamini-Hochberg adjusted FDR at p < 0.05) and non-significant genes (open
1382 circle) are shown.
- 1383 (F) Hierarchical clustering of the normalized composite central mean coverage at TFBSs
1384 from the Griffin analysis of ctDNA for 108 TFs in LuCaP PDX lines of ARPC (n=16),
1385 NEPC (n=6), and ARLPC (n=2) phenotypes. This list of TFs was initially selected as
1386 having differential expression between ARPC and NEPC from LuCaP PDX RNA-Seq
1387 analysis. Heatmap colors indicate increased accessibility (low values; yellow, orange,
1388 red) and decreased accessibility (higher values; black) in ctDNA. TFs with increased
1389 accessibility in NEPC samples (log₂-fold-change > 0.05, Mann-Whitney U test p < 0.05)
1390 are indicated with red bars; increased accessibility in ARPC (log₂-fold-change < -0.05, p
1391 < 0.05) are indicated with blue bars. Text color indicates relative expression between
1392 ARPC and NEPC PDX tumors by RNAseq shown for TFs with significant differential
1393 accessibility.

1394

1395 **Figure 4. Comprehensive evaluation of ctDNA features throughout the genome for CRPC**
1396 **phenotype classification in PDX models**

1397 (A) Volcano plot of \log_2 -fold change of ATAC-Seq peak intensity between 5 ARPC and 5
1398 NEPC lines; the dotted line demarcates sites by q -value < 0.05 .

1399 **(B-C)** Composite coverage profiles at open chromatin sites specific to ARPC **(B)** and NEPC
1400 **(C)** PDX tumors analyzed by Griffin. Sites from (A) were filtered for overlap with known
1401 TFBSs in 338 factors from GTRD (70). Coverage profile means (lines) and 95%
1402 confidence interval with 1000 bootstraps (shading) are shown. The region ± 150 bp is
1403 indicated with vertical dotted line and yellow shading.

1404 **(D)** PCAs of ctDNA features demonstrates grouping between ARPC and NEPC phenotypes:
1405 **(left)** Composite central coverage of TFBSs significant for 74 TFs with differential
1406 accessibility out of 338 factors between ARPC and NEPC (**Supplementary Table S4**).
1407 **(center)** NPS in the gene bodies of the 47 phenotype defining genes. **(right)** Fragment
1408 size variability (coefficient of variation) at H3K4me1 histone modification sites ($n=9,750$).

1409 **(E)** Performance of classifying ARPC vs NEPC PDX from ctDNA using supervised machine
1410 learning (XGBoost) in various region types (all genes, TFBSs, and open regions,
1411 **Methods**). Area under the receiver operating characteristic curve (AUC) with 95%
1412 confidence interval (100 repeats of stratified cross validation) is shown for performance
1413 of all feature types.

1414

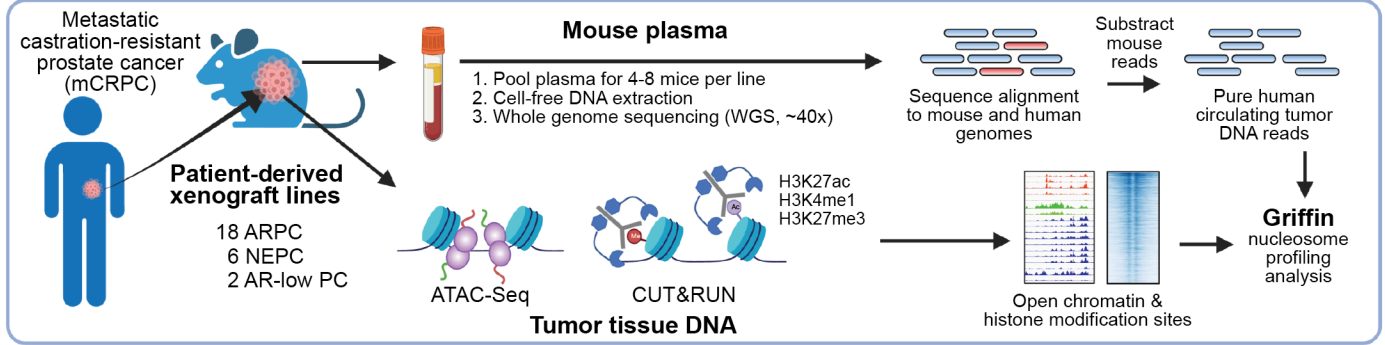
1415 **Figure 5. Accurate classification and estimation of prostate cancer in patient plasma**
1416 **samples**

- 1417 (A) Schematic illustration of the ctdPheno classification method. Griffin-derived features and
1418 ichorCNA tumor fraction estimates from patient plasma samples are combined in a
1419 probabilistic framework informed by PDX models to predict the presence of NEPC.
- 1420 (B) Performance for classification on admixtures samples using ctdPheno. Five ctDNA
1421 admixtures were generated for each phenotype from PDX lines, each at various
1422 sequencing coverages and tumor fractions. In total, 125 admixtures were evaluated. The
1423 mean AUC across the 5 admixtures is shown for each configuration.
- 1424 (C) Receiver operating characteristic (ROC) curve for 101 mCRPC patients (DFCI cohort I)
1425 with ultra-low-pass WGS (ULP-WGS) data. The optimal performance of 90.4%
1426 sensitivity (for predicting NEPC) and 97.5% specificity (for predicting ARPC)
1427 corresponding to a prediction score cutoff of 0.3314 is indicated with horizontal and
1428 vertical dotted lines, respectively.
- 1429 (D) Prediction scores from ctdPheno for 47 ULP-WGS plasma samples with clinical
1430 phenotypes comprising 26 ARPC (blue), 5 NEPC (red), and 16 mixed or ambiguous
1431 phenotypes (purple, triangles), including double-negative prostate cancer (DNPC; grey).
1432 The 0.3314 score cutoff threshold (dotted line) was used for classifying NEPC and
1433 ARPC. Tumor fractions were estimated by ichorCNA from WGS data.
- 1434 (E) Schematic illustration of the Keraon mixture estimation method. Griffin-derived features
1435 from PDX lines and healthy donors define a known feature space, which is transformed
1436 based on Griffin features and ichorCNA tumor fraction estimates for each patient plasma
1437 sample. Based on the patient's location in the transformed phenotype space, fractions of
1438 each phenotype are inferred directly.
- 1439 (F) Illustration of mixture simulations. 5 ARPC and 5 NEPC PDX samples were combined in
1440 the ratios shown with a single healthy donor at the tumor fractions shown, for a total of
1441 810 mixed phenotype samples at 25x for evaluating mixture proportions with Keraon.
- 1442 (G) Boxplot of predicted total NEPC fraction in 810 simulated mixed-phenotype samples
1443 using Keraon, Pearson's $r = 0.884$. Median absolute error (MAE) was computed as the
1444 median absolute difference between estimated and expected NEPC fraction across all
1445 samples.
- 1446 (H) Fractional phenotype estimates for 47 WGS plasma samples with clinical phenotypes
1447 comprising 26 ARPC (blue), 5 NEPC (red), and 16 mixed or ambiguous phenotypes

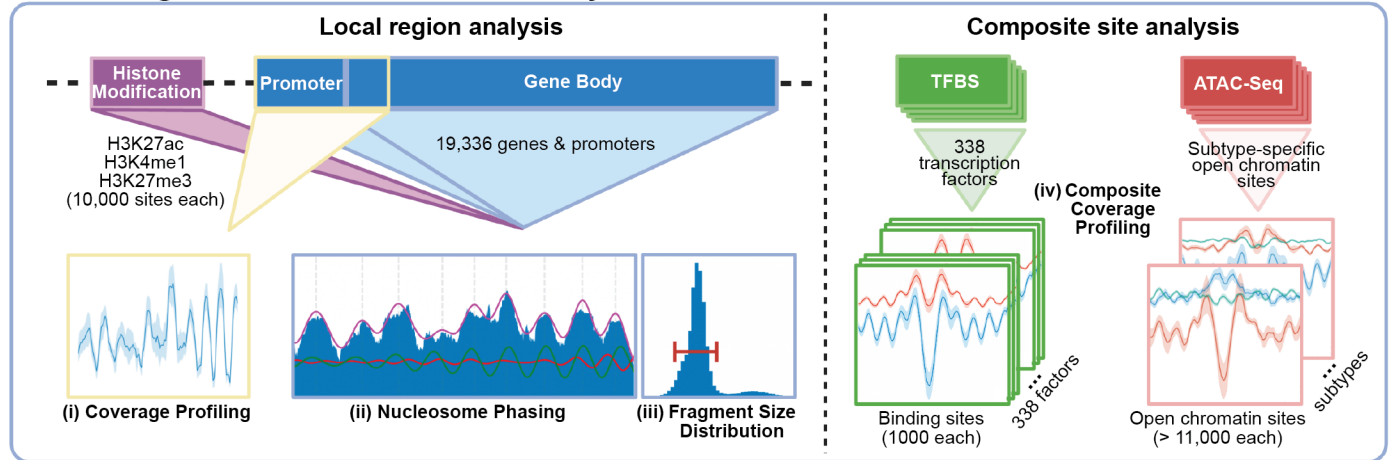
1448 (purple, triangles), including double-negative prostate cancer (DNPC; grey). The 2.8%
1449 NEPC fraction threshold indicates the predicted presence of NEPC (dotted line).
1450

A

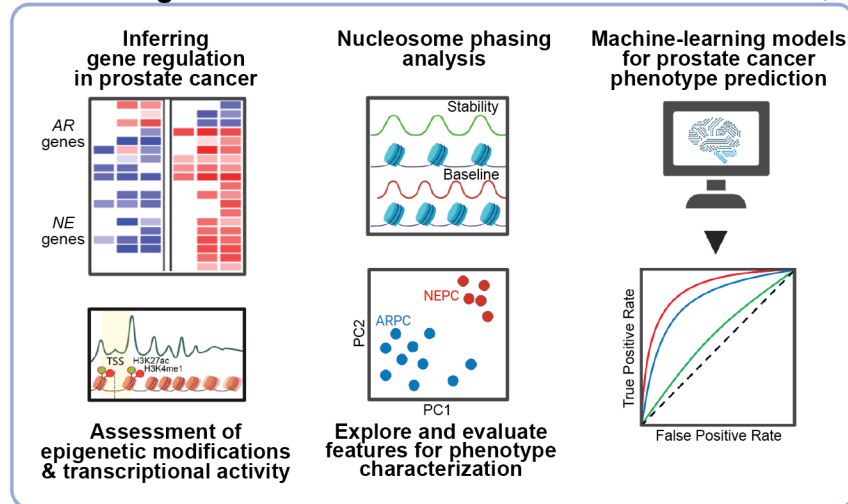
PDX Plasma and Tumor Sequencing



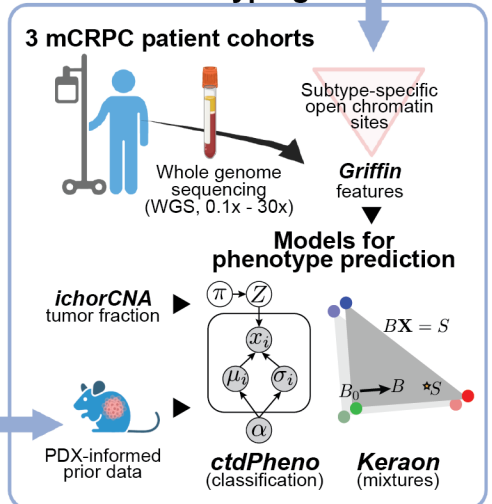
Circulating Tumor DNA Feature Discovery



Circulating Tumor DNA Characterization



Patient Phenotyping



B

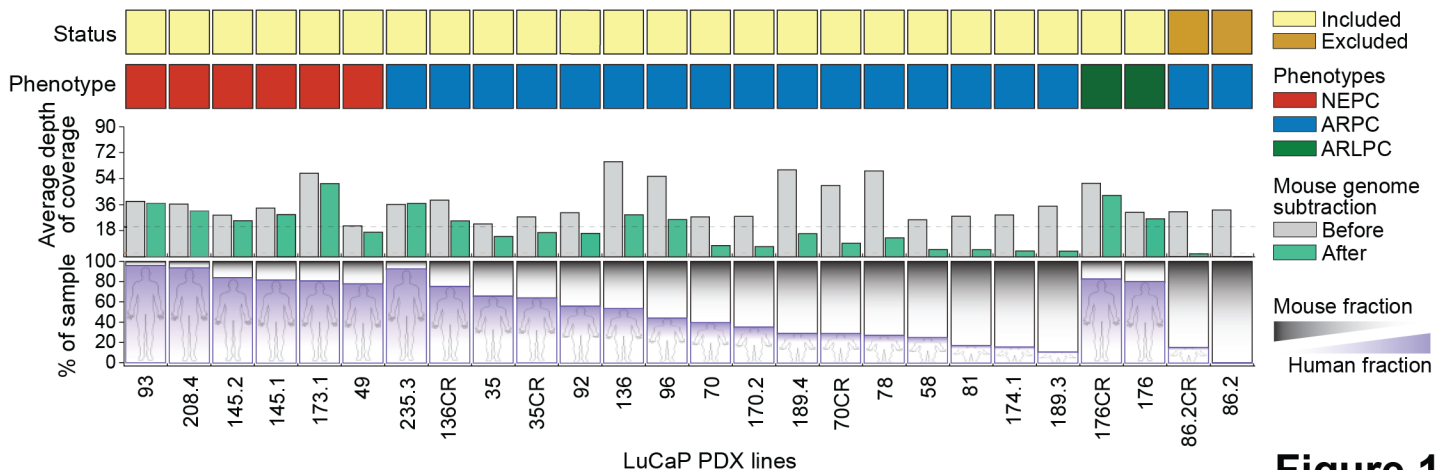


Figure 1

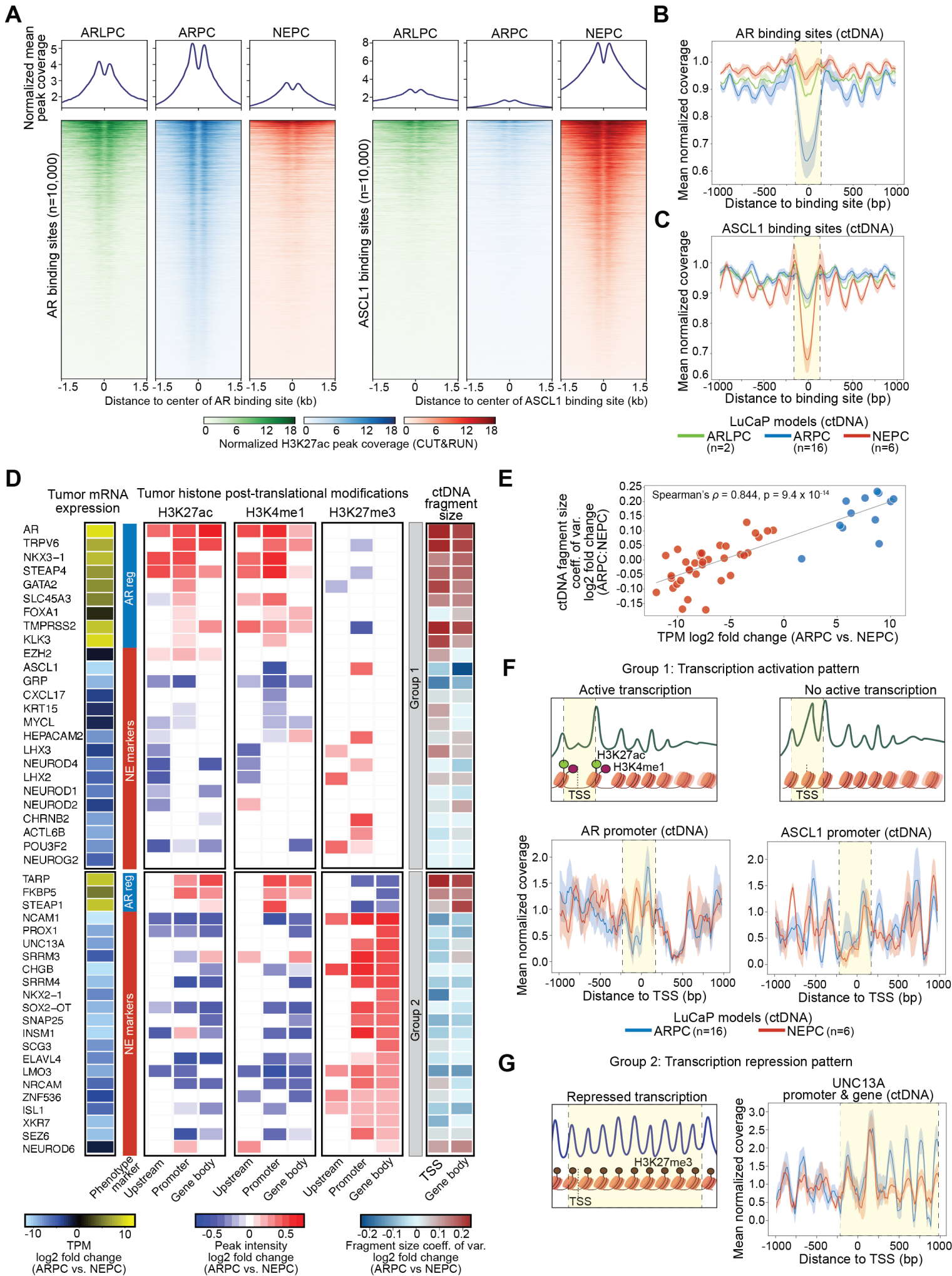
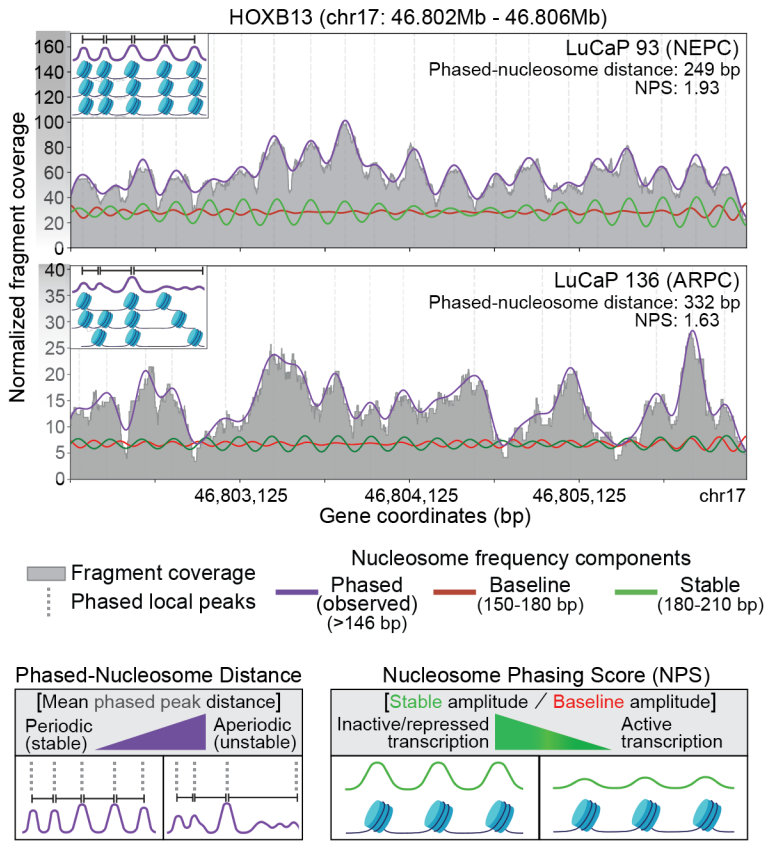
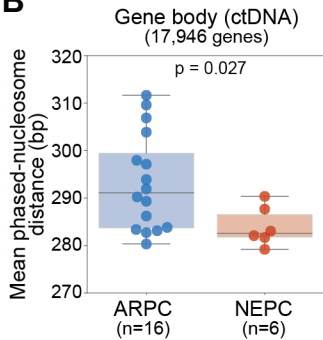


Figure 2

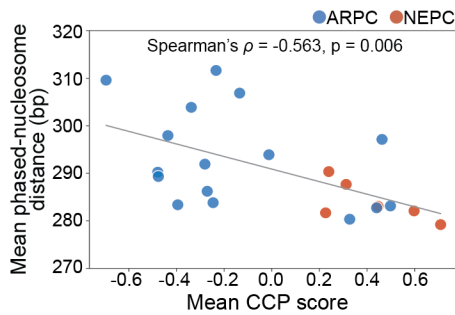
A



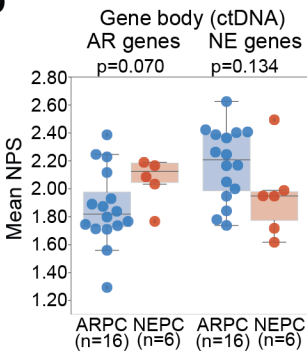
B



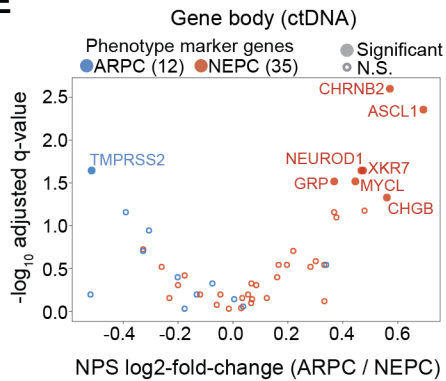
C



D



E



F

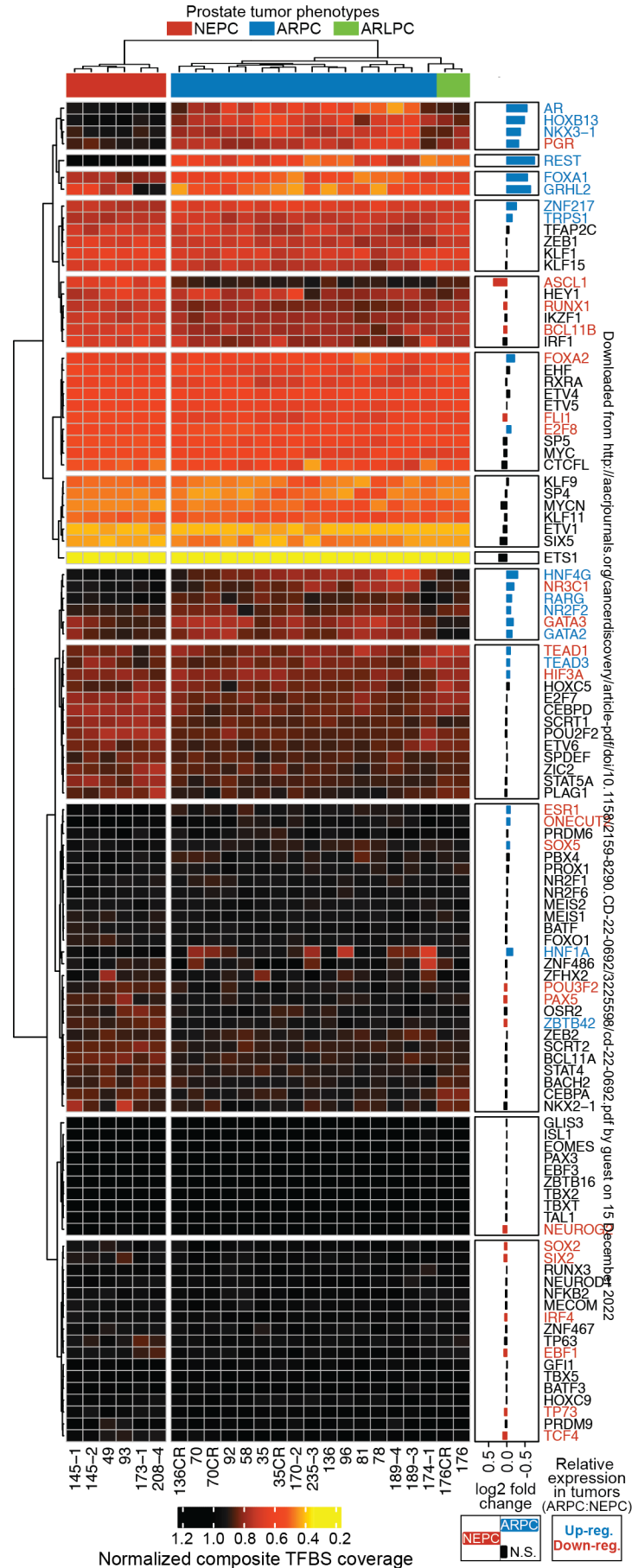


Figure 3

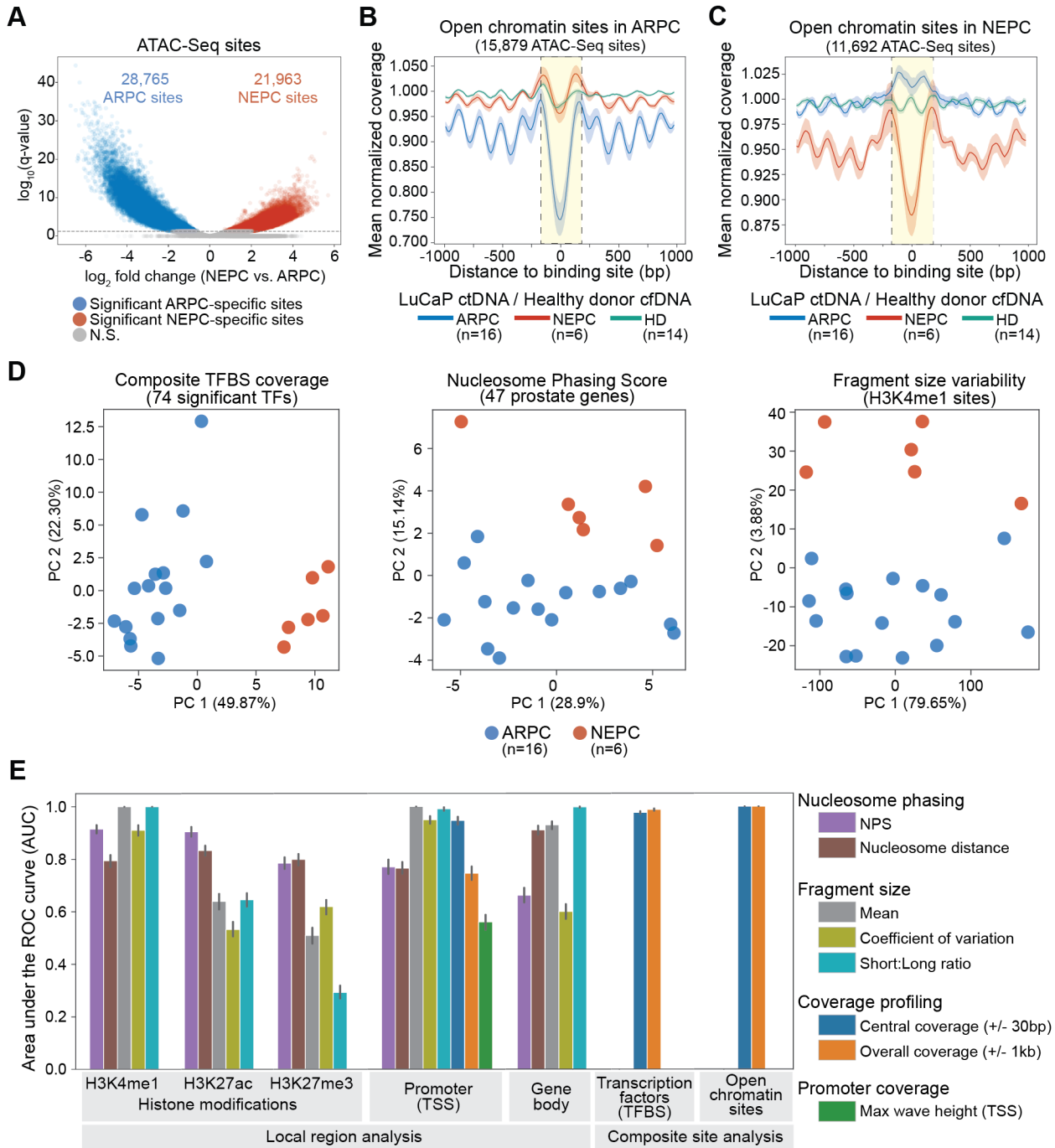


Figure 4

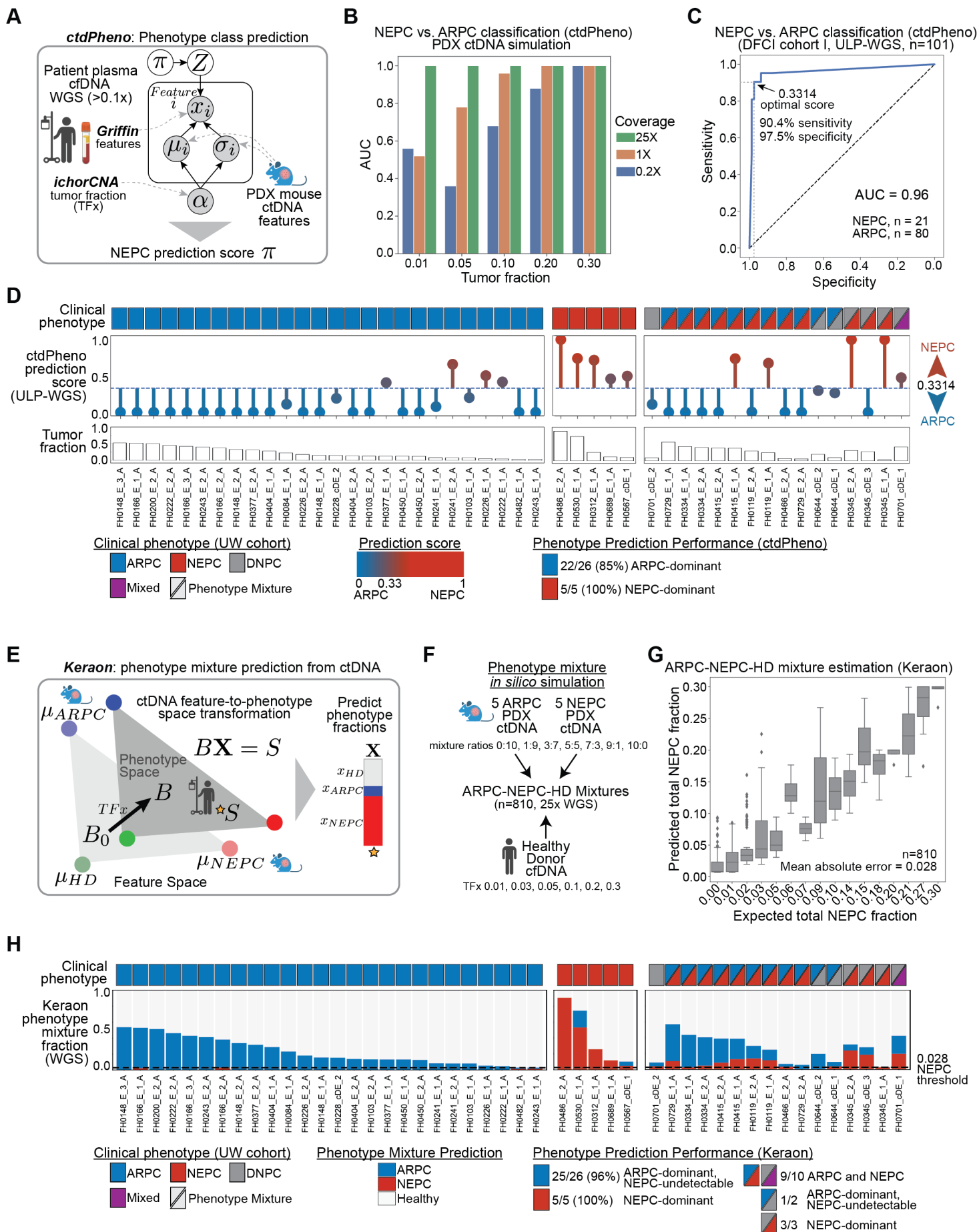


Figure 5